DIPLOMARBEIT

Plasma Edge Profiles and their Stability in the X-Point Radiator Regime at the ASDEX Upgrade Tokamak

ausgeführt am
Institut für Angewandte Physik
der Technischen Universität Wien
und am
Max-Planck-Institut für Plasmaphysik

unter der Anleitung von
Univ. Prof. Dr. Friedrich Aumayr
Univ. Prof. Dr. Elisabeth Wolfrum

durch
Luca Matteo Hofstadler, B.Sc.
Matrikelnummer: 01525923 | Studienkennzahl: 066 461

Wien, 25. Oktober 2023

_____   _____
Friedrich Aumayr   Luca M. Hofstadler

Abstract

Current research focuses on a possible future operating mode for magnetic confinement fusion devices that features excellent fusion conditions through the development of an edge-transport barrier (ETB), also called pedestal. The ETB causes plasma parameters to increase rapidly inwards from the plasma edge, forming steep gradients. These steep edge gradients in the high-confinement mode (H-mode) in turn feed magnetohydrodynamic (MHD) instabilities like edge localised modes (ELM) which expel large amounts of energy in a burst-like manner and therefore pose a threat for the longevity of the plasma-facing components. The high power flux exiting the plasma and funnelled into the divertor where it connects over a small area with the targets is predicted to generate a power load of >10MW/m^2, exceeding current material limits.

A phenomenon that is being studied at the ASDEX Upgrade tokamak is the X-point radiator (XPR) which is a small, poloidally localised radiating volume situated above the X-point and inside the confined region. The XPR is developed through means of large gas puff fuelling and impurity seeding, and its position can be actively controlled. The radiation has a power fraction of around 95-100%, hence substantially reducing the power exhaust and the temperature in the divertor, allowing for divertor detachment and a safe operation. In addition, it was discovered that the plasma can enter an ELM-free regime with negligible plasma degradation if the XPR height exceeds a certain threshold. This opens up the possibility of a scenario in which the plasma could be operated safely and within material limits.

One aim of this thesis was to study the change in various plasma parameters with respect to the XPR height. The analysis focused on the edge profiles and their gradients, because of their known influence on the confinement. The other task was to investigate the peeling-ballooning (PB) stability of the edge profiles as the plasma becomes ELM-free.

Throughout the analysis, a total of 95 time windows of 225 ms length of 7 discharges were selected for the database. The selection of discharges was limited to 800 kA at 2.5 T, as the largest range of XPR positions could be achieved experimentally in this configuration. The measurements of several electron and ion property diagnostics were utilised in a standardised integrated data analysis (IDA) approach to generate the plasma parameter profiles. The subsequent plasma parameter analysis consisted of examining the plasma parameter (X), its gradient (∇X) and gradient length ($X/\nabla X$) and their behaviour on the XPR height in four different subregions in the radial region $\rho_{\mathrm{pol}} \in [0.7 - 1]$. For better comparison the reference value was determined at an XPR height of 0 cm. In terms of the MHD stability analysis, the codes HELENA and MISHKA provided calculations on the ballooning and PB stability.

The investigation showed that the electron and ion temperature profile in the pedestal decrease linearly with XPR height and that the transition from ELMy to ELM-free regime is without significant change in behaviour. Although the pedestal degrades, the profiles are able to recover within the investigated region due to changes in gradients inside the pedestal. This was found to only hold true up to an XPR height of around 7 cm after which the plasma degrades below the reference. In addition, it was discovered that the electron density peaked at an XPR height of 4-5 cm, coinciding with a partial detachment of the divertor. The MHD analysis can confirm and explain the disappearance of ELMs due to the

decrease of the experimental normalised pedestal pressure gradient below its critical value and the subsequent shift of the operational point in the MHD stability phase space away from the ballooning boundary towards the stable region.

Zusammenfassung

Die derzeitige Forschung konzentriert sich auf einen möglichen Betriebsmodus für zukünftige Fusionsanlagen (welche auf dem magnetischem Einschluss Prinzip basieren), der durch die Entwicklung einer Randtransportbarriere (ETB), auch genannt "Pedestal", hervorragende Fusionsbedingungen bietet. Diese ETB bewirkt, dass die Plasmaparameter von der Separatrix aus rasch ansteigen und steile Gradienten bilden. Die steilen Randgradienten in der Hocheinschlussmode (H-Mode) führen wiederum zu großen magnetohydrodynamischen (MHD) Instabilitäten, wie z. B. lokalisierten Randmoden (ELM), welche große Energiemengen explosionsartig ausstoßen und daher ein Problem für die Langlebigkeit der plasmazugewandten Komponenten darstellen. Ein weiteres Problem ist der hohe Leistungsfluss aus dem Plasma, der in den Divertor geleitet wird, welcher dort auf eine lediglich kleine Fläche trifft und somit eine Leistungsbelastung von $> 10 \mathrm{MW/m^2}$ erzeugt, die die derzeitigen Materialgrenzen überschreitet.

Ein Phänomen, das bei ASDEX Upgrade untersucht wird, ist der X-Punkt-Strahler (XPR), ein kleines, poloidal lokalisiertes Strahlungsvolumen, das sich oberhalb des X-Punkts und innerhalb des eingeschlossenen Bereichs befindet. Der XPR wird durch das Einblasen von Verunreinigungen erzeugt - seine Position lässt sich aktiv steuern. Die Strahlung des XPR beträgt etwa 95-100% der eingeführten Leistung, wodurch der Leistungsabfall und die Temperatur im Divertor erheblich reduziert werden, was einen sicheren Betrieb ermöglicht. Darüber hinaus wurde festgestellt, dass das Plasma bei einer XPR-Höhe von 7 cm über dem X-Punkt ELM-frei ist bei lediglich milder Plasmaeinschlussverminderung. Dies eröffnet die Möglichkeit eines Betriebsmodus, in dem das Plasma sicher und innerhalb der Materialgrenzen betrieben werden kann.

Ein Ziel dieser Arbeit war es, die Veränderung verschiedener Plasmaparameter in Abhängigkeit von der XPR-Höhe zu untersuchen. Die Analyse konzentrierte sich auf die Randprofile und deren Gradienten, da bekannt ist, dass diese einen großen Einflusses auf den Einschluss haben. Die andere Aufgabe bestand darin, die Peeling-Ballooning-Stabilität (PB) der Randprofile zu untersuchen, wenn das Plasma einen ELM-freien Zustand erreicht.

Während der gesamten Analyse wurden insgesamt 95 Zeitfenster von je 225 ms Länge in 7 Entladungen für die Datenbank ausgewählt. Die Wahl wurde auf Entladungen mit 800 kA bei 2.5 T beschränkt, da bei diesen Werten die größte Auswahl an Entladungen mit einem XPR existiert. Die Messungen mehrerer Elektronen- und Ioneneigenschaftsdiagnosen wurden in einem standardisierten Ansatz zur integrierten Datenanalyse (IDA) kombiniert um folglich die Plasmaparameterprofile zu erstellen. Die anschließende Analyse der Plasmaparameter bestand aus der Untersuchung des Plasmaparameters (X), seines Gradienten (∇X) und der Gradientenlänge ($X/\nabla X$) und deren Verhalten auf die XPR-Höhe in vier verschiedenen Unterregionen im radialen Bereich $\rho_{\mathrm{pol}} \in [0,7-1]$. Um einen besseren Vergleich zu gewährleisten, wurden die Werte bei einer XPR-Höhe von 0 cm als Referenzwert gewählt. Im Rahmen der MHD-Stabilitätsanalyse wurden mit den Codes HELENA und MISHKA Berechnungen zur Ballon- und PB-Stabilität durchgeführt.

Die Untersuchung ergab, dass das Elektronen- und Ionentemperaturprofil im Pedestal linear mit der XPR-Höhe abnimmt und dass der Übergang vom ELMy- zum ELM-freien Regime ohne signifikante Änderung des Verhaltens erfolgt. Obwohl sich die Werte des Pedestals verschlechtern, können sich die Profile innerhalb der untersuchten Region aufgrund von Änderungen der Gradienten der Bereiche innerhalb des Pedestal erholen. Dies gilt jedoch nur bis zu einer XPR-Höhe von etwa 7 cm, danach sinkt das Werte unter jene der Referenz ab. Darüber hinaus wurde festgestellt, dass die Elektronendichte bei einer XPR-Höhe von 4-5 cm ihren Höhepunkt erreicht, was mit einem teilweisen "Detachments" des Divertors zusammenfällt. Die MHD-Analyse kann das Verschwinden der ELMs aufgrund der Abnahme des experimentellen normalisierten Pedestaldruckgradienten unter seinen kritischen Wert und der anschließenden Verschiebung des Betriebspunkts im MHD-Stabilitätsphasenraum weg von der Ballongrenze hin zum stabilen Bereich bestätigen und erklären.

Contents

Chapter 1

Introduction

The world population is growing and so is its thirst for energy. Unfortunately, these demands are usually met by using fossil fuels. Due to that, humankind has emitted over 2420 ± 240 Gt of CO_2 since the industrial revolution and therefore increased the atmospheric concentration by over 50%.[1] Because of this emission, the natural green house gas effect got amplified, leading to a temperature rise of already ~1°C.[2] Figure 1.1 demonstrates the correlation between accumulated CO_2 emissions and the warming of our planet through an almost linear trend. The figure also presents projections of several scenarios which factor in how fast our world acts against global warming. These range from an optimistic maximum increase of 1.3 °C to a disturbing 3 °C. The change of our climate has already begun and will inevitably lead to an even bigger rise in number and severity of abnormal weather phenomena such as draughts, floods, hurricanes and urban heat waves, an increase of the sea level and a drastic reduction of wildlife diversity. These are just some effects that the planet will experience. Humanity will have to deal with several other issues than just hotter climate.

The increase in likeliness of extreme weather events will ultimately lead to more crop failure, which will consequently lead to conflicts and mass migrations in the developing world. Research conducted in 2019 showed that global warming increased the armed conflict risk by 3-20% over the last 100 years.[3] . The United Nations Environment Programme concluded that the war in Darfur(Sudan) is driven by the climate crisis and stated that this issue could be a spark for several new conflicts in Africa.[4] Through droughts and bad harvest, rural workers are forced into cities to be able to provide for themselves and their families, triggering conflicts via overpopulation and mass unemployment. These circumstances will leave people prone to recruitment by radical armed groups (e.g. the Islamic State and Boko Haram).

Furthermore, with the decrease in natural habitat and warmer conditions in previously colder parts of the planet, the world will see an increase in exotic diseases. An example is the warm water cycle el Niño, which is influenced by the warmer climate. This natural phenomenon is linked to a rise in mosquito transmitted diseases in Colombia and Venezuela such as malaria, dengue, and Rift Valley fever.[5] It is very likely (but not certain) that these illnesses will make it to Europe, the US and other temperate climate regions. Unfortunately, these areas are extremely vulnerable and often unprepared for these events as could be seen in the COVID-19 pandemic.

These are just some examples why mankind should be motivated to fight global warming. Therefore, investing in carbon-free energy sources should be mankind's highest priority. Luckily, there are already a lot of possibilities to generate green energy, but they often lack in consistent and reliable power production. Due to that a baseline energy generating source
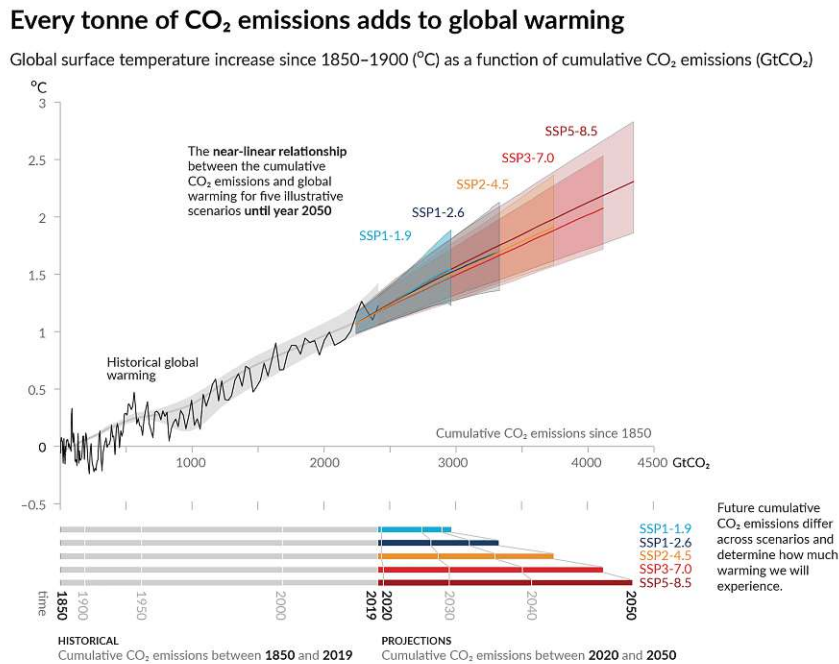
Every tonne of CO₂ emissions adds to global warming

Global surface temperature increase since 1850–1900 (°C) as a function of cumulative CO₂ emissions (GtCO₂)

Figure 1.1: Figure SPM.10 in IPCC, 2021: Summary for Policymakers. Relationship between human emitted CO_2 and global surface temperature increase plus projections on five possible CO_2-reduction scenarios. Adapted from [2].

has to be found, capable of delivering a huge power output with a short response time. Although nuclear fission power plants could solve this issue, they pose an environmental risk and even with safe operation have the downside of producing huge quantities of long-lived highly radioactive waste. An energy source that could meet all demands is nuclear fusion. It could consistently and reliably provide power, does not pose a safety risk when in operation and its activated components decay to a safe level within 100 years.[6]

1.1 Nuclear Fusion

Nuclear fusion occurs when two or more atomic nuclei interact, overcoming their initial repulsion and forming a heavier nucleus. During this process, a decrease in mass between the sum of the reactants and the products occurs. Through the famous $E = mc^2$ equation it is known that mass and energy are equivalent. In this case, this means that the mass deficit is converted into kinetic energy of the fusion product particles. The mass difference is also stored in the fusion product as the so-called binding energy. This specific energy is negative, meaning that energy has to be invested to separate the nuclei.

The release of energy through fusion is very energetic and is the driving force in what keeps the sun and other stars burning. The mechanism happening in the sun is called proton-proton chain.[7] It involves protons (hydrogen) which under several different steps fuse into helium under the emission of huge amounts of energy. This process takes place using the weak interaction to transform protons into neutrons, which due to its very small reaction cross-section and the small energy density taking millions of years to be initiated. Due to that, another fusion process has to be chosen to drive future power plants.

Since the most time consuming step in the proton-proton chain is the production of deu-

terium, the choice for a more feasible fusion reaction to use on earth would be to involve deuterium from the very start.[8] Luckily, this isotope is relatively abundant on earth with a 1 : 6700 ratio of deuterium to hydrogen. It can either react with itself fusing into a helium-3 atom plus a neutron or forming a tritium nucleus plus a proton.

$$\begin{array}{ccc} {}_1^2\text{D} + {}_1^2\text{D} & \longrightarrow & {}_1^3\text{T} + {}_1^1\text{p} + 4.04\,\text{MeV} \\ & \searrow & {}_2^3\text{He} + {}_0^1\text{n} + 3.27\,\text{MeV} \end{array}$$
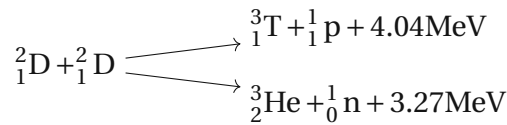
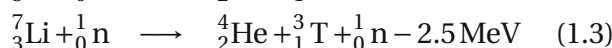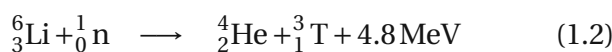These fusion products can then also react with deuterium again forming new fusion scenarios. However, initially these nuclei repel each other due to the Coulomb force, which they have to overcome for the strong interaction to set in. This means that for fusion to happen, the reactants have to carry enough kinetic energy to overcome the Coulomb barrier, or due to the quantum tunnel effect only a fraction of it. The Maxwell-Boltzmann averaged reactivity $\langle \sigma v \rangle$ (explained further down in this section) of this process, in dependence of the particles' temperature can be seen in fig. 1.2.

As it turns out, the reactivity of deuterium-tritium-fusion (subsequently abbreviated as DT-fusion) is several magnitudes higher at lower temperatures than DD- or DHe3-fusion. Unfortunately, tritium is not a naturally occurring isotope on earth, since its half-life is of around 12.3 years. This means in order to utilise DT-fusion, tritium has to be produced artificially. This is done through lithium.

Figure 1.2: The Maxwell-Boltzmann-distribution-averaged fusion reactivity for several fusion reactions in dependence of the reactants' temperature. Adapted from [9].

The products of the DT-fusion are a helium-4 atom and a neutron under the release of 17.6 MeV. Due to the conservation of energy and momentum the neutron carries the majority of that energy with 14.1 MeV and the helium-4 the remaining 3.5 MeV.

$$ {}_1^2\text{D} + {}_1^3\text{T} \quad \longrightarrow \quad {}_2^4\text{He} + {}_0^1\text{n} + 17.6\,\text{MeV} \qquad (1.1) $$
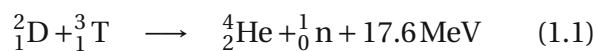
This neutron has to be absorbed by a lithium atom, in order to then decay and produce a tritium. The process depends on which lithium isotope captures the neutron.

$$ {}_3^6\text{Li} + {}_0^1\text{n} \quad \longrightarrow \quad {}_2^4\text{He} + {}_1^3\text{T} + 4.8\,\text{MeV} \qquad (1.2) $$
$$ {}_3^7\text{Li} + {}_0^1\text{n} \quad \longrightarrow \quad {}_2^4\text{He} + {}_1^3\text{T} + {}_0^1\text{n} - 2.5\,\text{MeV} \qquad (1.3) $$

The natural abundance of lithium consists of 6.4% Li-6 and 92.4% Li-7. Li-6 releases 4.8 MeV and has its highest probability with slow neutrons, whereas the Li-7 reaction consumes 2.5
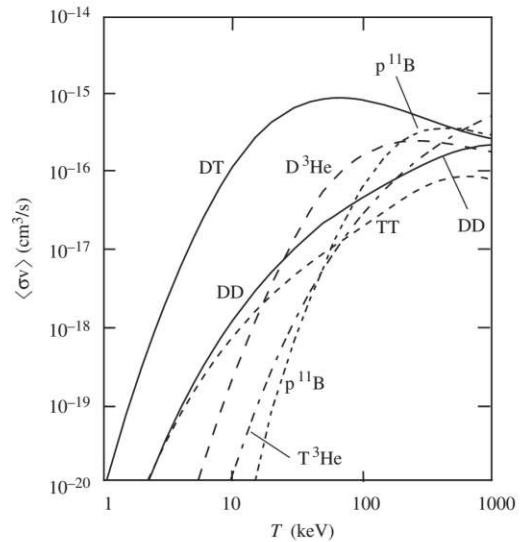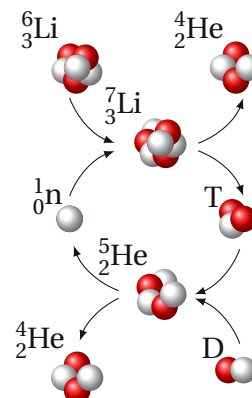

Figure 1.3: Complete DT-fusion reaction plus the breeding of tritium through lithium decay.

MeV, meaning that it is only possible with a fast neutron. Fortunately, the released neutrons from the DT-fusion are carrying ~14 MeV, which means that each isotope can contribute. Figure 1.3 shows an illustration of the whole DT-fusion process with incorporated tritium breeding.

This means a fusion reactor must not only generate temperatures hotter than the sun's surface, the reactants also have to be enclosed in a volume to enhance their chances of getting in contact with one another. Since any material vaporises above 3000 K, the plasma must not come in contact with the wall. This is where the ionised state of the fusion reactants is advantageous. Magnetic confinement is a method where the trajectory of the particles is controlled via magnetic fields. It is one of two major fusion concepts. The other one is inertial confinement, where the fuel is heated and compressed so fast that fusion takes place before the fuel can interact with the wall. This work focuses on magnetic confinement devices.

1.2 Magnetic Confinement Fusion Device

As previously described, a magnetic field is used to control the motion of the fusion reactants in the device of interest. In order for the particles to not escape the field, they can be trapped using a magnetic mirror or via a machine that uses a ring shaped field. The second option proved to be more feasible with less particle-escape.

From the beginning, many ideas on how to realise such a device were conceived, but in 1968 the former Soviet Union presented data of its concept which lead to a global trend towards their design, the so called *Tokamak*. A Russian acronym ("toroidal'naya kamera s magnitnymi katushkami") meaning toroidal chamber with magnetic coils. Figure 1.4 shows a simple diagram of such a machine. The construct consists of three major parts which are the vacuum vessel, toroidal field coils and central solenoid.
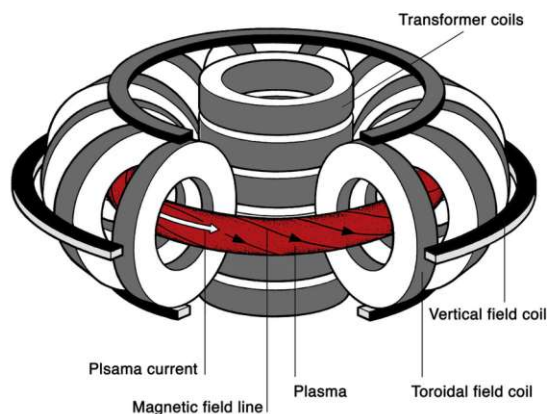
Figure 1.4: Diagram of a tokamak fusion reactor with its magnetic field generating components. Adapted from [10]. Copyright: MPI for Plasma Physics

The torus-shaped containment vessel contains the plasma and allows for a lower pressure inside, so that a discharge can be ignited more easily. Toroidal field coils are set up alongside the torus, generating a toroidal magnetic field which purpose it is to keep the hot plasma away from the wall. The charged particles are hence bound to travel along these field lines.

However, the toroidal magnetic field is not homogeneous. It is strongest in the middle of the torus and decreases towards the outside. This magnetic gradient, in combination with the curvature on the field lines, generates an opposing vertical drift for the differently charged particles. Through charge separation, an electric field develops which creates an outwards directed radial drift for particles regardless of charge, causing a plasma degradation.

To counteract the particle escape, a second magnetic field is generated to create helical field lines which allow for a short circuit of the vertical charge separation. This auxiliary magnetic field is achieved through the central solenoid. This component induces a current in the plasma, because it acts as a transformer where the second loop is the plasma itself.

The generated current produces a poloidal magnetic field which in combination with the toroidal field forms a helical one. These field lines form flux surfaces as they run around the torus. In the tokamak the toroidal field is typically 10-times greater than the poloidal one. Poloidal field coils are added to the system to manipulate the position of the plasma and act against effects that push the plasma column outwards.

A poloidal cross-section of the magnetic system reveals a system of nested tubes which are centered around the magnetic axis and bounded by the last closed flux surface (LCFS). The LCFS originates either from a physical object, which limits the radial expansion in a so called limiter configuration, or the magnetic field is manipulated in a way that there are closed and open field lines (see fig. 1.5). The open field lines are manipulated so that they connect with the material of the vacuum vessel in the divertor region. The material used in that area has to be capable of withstanding high power loads (e.g. tungsten) because the LCFS carries a high energy and particle flux. Many devices apply the second option because it introduces less impurities into the plasma and allows for a better confinement. For this type of magnetic configuration the LCFS is called separatrix.
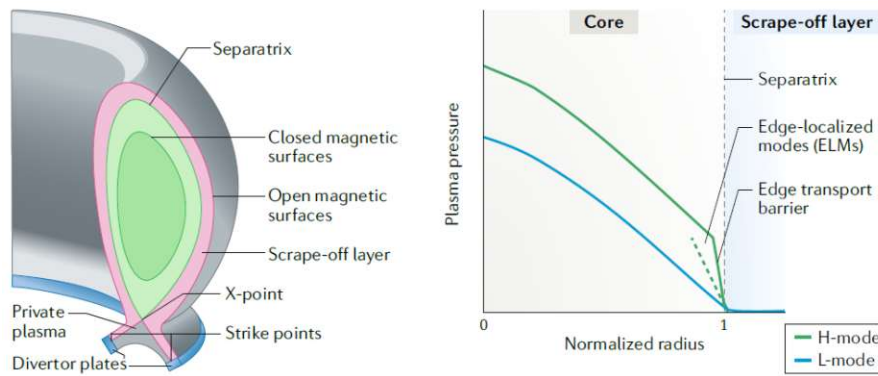
Figure 1.5: (Left) Poloidal cross-section of a tokamak with divertor in lower single null configuration. (Right) Radial pressure profile in different confinement modes (see section 2.1) plotted over ρ_{pol}. Adapted from [11].

Another part of interest is the X-point (displayed in fig. 1.5). In current tokamak configurations the magnetic field is manipulated so that the intersection of plasma and wall is further away from the confined region. To achieve this circumstance a concentric toroidal coil carries a current parallel to the plasma current I_{p}. The resulting magnetic field forms a figure-of-eight shape in the poloidal plane which is cut by the divertor region. The X-point is the location at which the poloidal magnetic field is null.

On closed flux surfaces particles exchange energy almost instantaneously, resulting in an immediate dissipation of temperature or density fluctuations. Therefore, a constant pressure prevails over a tube. Since a lot of properties are equal on a flux surface, it is common to use a variable to describe the radial dependence of quantities which has its centre at the magnetic axis and is normalised to the LCFS. This coordinate is often ρ_{pol} and is defined as follows:

$$\rho_{\text{pol}}(\Psi) = \sqrt{\frac{\Psi - \Psi_{\text{axis}}}{\Psi_{\text{sep}} - \Psi_{\text{axis}}}} \tag{1.4}$$

with Ψ being the poloidal flux, Ψ_{axis} the flux at the magnetic axis and Ψ_{sep} the one at the LCFS (here separatrix). An example of a pressure profile with ρ_{pol} dependence in a high confinement mode (see section 1.4) is shown in fig. 1.5.

1.3 ASDEX Upgrade

The tokamak is one of the most applied and well-understood concepts for magnetic confinement fusion devices. This is why an international project funded by 35 states invested into this design, building the International Thermonuclear Experimental Reactor or *ITER*. This machine is one of the most ambitious international science undertakings and it will be the biggest fusion experiment in the world.[12]

Its purpose is to demonstrate that fusion power can be successfully harnessed, so that it can be the predecessor of DEMO, a first commercial fusion power plant. In the process of building it, the knowledge and information gathered from other tokamaks is essential. The Max Planck Institute for Plasmaphysics (IPP) situated in Garching (Germany) is operating such a device and is contributing essential findings (especially with respect to plasma turbulences, the divertor, wall materials and many more[13]) towards ITER. This tokamak is called ASDEX Upgrade (AUG) and is the source of the data used in this work. It is the acronym of axisymmetric divertor experiment and it was built in 1991 as an upgrade to the original AS-DEX. The device is 9 m tall, has a major plasma radius of 1.6 m and a minor radius of 0.5 m, which accounts for a plasma volume of ~13 m^3.[14] It was designed for a magnetic field of 3.9 T and for a plasma current of 2 MA. A discharge can then be sustained for ~ 10 s and is observed by roughly 40 different diagnostics.

Figure 1.6: Diagram of ASDEX Upgrade with its supporting structure (red), main field coils (bronze), vacuum vessel (silver) and plasma (purple). Adapted from [15].
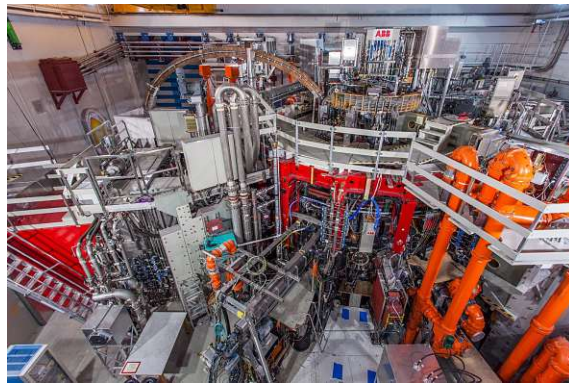
Figure 1.7: Photo of ASDEX Upgrade. Most of the device is covered by diagnostics and auxiliary systems with only the supporting structure being visible. Adapted from [15].

Additional heating is provided through 20 MW neutral beam injection heating (NBI), a maximum of 6 MW ion-cyclotron resonance heating (ICRH), a maximum of 8 MW electron-cyclotron resonance heating (ECRH) and 1 MW ohmic heating. However, the machine is only operated with up to 27 MW total heating power. The hydrogen or deuterium plasma can then be brought up to temperatures of ~ 100 mio. degrees and densities of around 2×10^{20} m^{-3}. To avoid excessive neutron activation, the use of tritium is omitted.

1.4 Current Obstacles: ELMs and Power Exhaust

There are two major regimes of operation at ASDEX Upgrade. They are differentiated by their level of confinement as the low confinement - (L-Mode) and high confinement mode (H-Mode) (see fig. 1.5). The second one is achieved when a certain heating threshold is surpassed, which was discovered by Fritz Wagner and his team in 1982 at ASDEX. It is the

preferable one for future fusion power plants, because it offers an operational regime with higher density and temperature resulting in a twice as high plasma confinement time than L-mode.[16] This is the result of sheared poloidal flow establishing an edge transport barrier which subsequently decreases turbulences causing less energy and particles to escape the confined region.[17] As the confinement enhances, steep gradients at the plasma edge form raising the pressure profile onto a pedestal.

These gradients are the source of energy for magnetohydrodynamic (MHD) instabilities such as edge localised modes (ELMs).[18] These are quasi-periodic relaxations of the edge transport barrier. They expel large amounts of energy and particles from the plasma, severely decreasing the pressure profile (see fig. 2.1) and damaging the vessel wall. As they scale with the size of the fusion device, their presence poses a significant danger for bigger devices such as ITER.

As mentioned in section 1.3, the field lines in the region beyond the LCFS (called Scrape-Off Layer or SOL) connect to the material of the vessel. The heat and particle flux carried by them into the divertor, can exceed material limits of 10 MW/m^2 in steady state operation which means 95% of the incoming power has to be dissipated for DEMO.[19, 20] A way of decreasing the flux is through controlled seeding of impurities such as Argon, Nitrogen and others (see section 2.3.5). As these gases are met by the incoming heat flux, they dissipate the energy into radiation and thereby take off load of the divertor tiles. This will be a necessary measure for ITER and DEMO.[21, 22]

1.5   Aim of the Thesis

ELMs and the high heat and particle flux are major challenges for a safe operation of large fusion devices. These obstacles could be overcome through the development of a stable X-point Radiator (XPR) in a discharge which creates an ELM-free regime.[23] The XPR is a small, poloidally localised radiating volume situated above the X-point and inside the confined region and is created by means of the seeding of impurities. Through it, it is possible to achieve full detachment of the divertor and radiate away 95% of the upstream power which was demonstrated through SOLPS-ITER simulations.[24] Additionally, several experiments conducted at AUG and JET (Joint European Torus, UK), confirmed an ELM-free regime under high impurity seeding.[25]

The main goal of this thesis is to analyse the reaction of the plasma to the presence of an XPR. Several plasma parameter profiles were examined with focus on their recovery from pedestal to core. The change in intensity and frequency of ELMs was studied with increasing XPR height. In addition to that, a peeling ballooning analysis was carried out to determine the operational point in the stability diagram ($\vec{j}$ vs α).

The thesis is subdivided into the following chapters:

Chapter 2 discusses MHD instability, the power exhaust and the current state of research of the X-point Radiator regime,

Chapter 3 introduces and describes the utilised diagnostics and advanced measurement techniques that were used in order to obtain the data,

Chapter 4 lists the discharges that were examined within the scope of this theses,

Chapter 5 deals with the workflow and methodological approach of the plasma parameter and plasma stability analysis,

Chapter 6 presents the data analysis and findings, and

Chapter 7 summarises the results and gives an outlook on possible future research.

Chapter 2

Theoretical Background of the X-Point Radiator

The following part addresses the subjects of ELMs (MHD instabilities) in H-Mode, the power exhaust mitigation mechanism and the formation of an X-point radiator via deliberate impurity seeding and its current physical description.

2.1 Magnetohydrodynamic Analysis of Edge Plasma Modes

The general description of Magnetohydrodynamic Analysis of Edge Plasma Modes and other topics throughout this section are based on the following publications [26, 27, 28, 29].

Since its first observation in 1982, the H-mode has been the primary focus of operation in nuclear fusion research reactors. Before that, tokamaks were operated in what was later characterised as L-mode. In L-mode edge turbulences develop unhindered and cause enhanced transport. The fact that core plasma conditions are determined by the boundary (particle and energy source/sink) therefore leads to a limitation in maximum achievable density and temperature. However, with the injected energy exceeding a certain threshold, a sudden formation of steep pressure gradients at the plasma edge occurs. Due to the relatively small extent of this region (1-2 cm in devices of 1-2 m major radius), it seems as if the radial pressure profile is placed upon a "pedestal" (see fig. 1.5).[11]

The position of the "pedestal top" is where the steep gradients become flatter. The gradients are a result of an edge-transport barrier (ETB) that allows for better confinement. The mechanism of the turbulence-suppression is believed to be enhanced shear flow due to a change of the radial electric field near the separatrix.[17, 27, 31]

Since H-mode is considered to be the preferred operational mode of future nuclear fusion power plants, one of its biggest drawbacks (the edge localised mode) has to be addressed. As briefly discussed in section 1.4, the steep edge gradients feed MHD instabilities causing heat and particle expulsion - and the pedestal is lowered. Afterwards the pressure profile and its gradients recover, facilitating a new ELM onset and completing the ELM cycle. An example of the pressure profile loss during an ELM cycle is displayed in fig. 2.1.

Figure 2.1: H-mode radial pressure profile with indicated pressure loss through ELMs. Adapted from [30].

Although they might prevent the accumulation of impurities and helium ash in the core, the rapidly released amount of energy of each ELM can be of 10% of the confined plasma energy.[26] This leads to a sudden time-averaged energy loss of ~10-20%, which despite considering the fast heat loss might be manageable, but its abrupt deposition on the target tiles and the henceforth induced damage is profound. These ELMs are categorised as Type-I ELMs (the biggest type) and have a frequency of 1-100 Hz. Other types of ELMs cause less plasma degradation and are subsequently referred to as "small ELMS".

2.1.1 Peeling-Ballooning Theory

In order to assess the edge plasma stability, the MHD energy functional is analysed. In this equation, it is the radial pressure gradient dp/dr and the parallel current density $j_{0\parallel}$ that are the two main drivers for instability. Two of the main instabilities that are proportional to these quantities are the ballooning (pressure gradient) and peeling (current) instability. Combined they form the most widely accepted theory about the origin of ELMs - the peeling-ballooning theory (PB Theory).[32, 33] It is built upon the coupling of ballooning and peeling modes through reaching a critical edge pressure gradient and edge current density.

Current Driven Instability

As it was mentioned in section 1.2, a plasma current I_p is induced to create a poloidal field, therefore twisting the field lines and preventing excessive particle loss. However, I_p has an upper limit as the attenuation of current instabilities relies on the relative strength with respect to the toroidal field. Two current driven instabilities are displayed in fig. 2.2.

The sausage instability can develop if a poloidal narrowing occurs. With the poloidal field $\boldsymbol{B_\theta}$ being inversely proportional to the minor plasma radius a this creates a higher magnetic- than kinetic-pressure. μ_0 being the vacuum permeability.

$$\boldsymbol{B_\theta}(a) = \frac{\mu_0 I_p}{2\pi a} \tag{2.1}$$

The plasma will then level the force imbalance by adverting the pressure difference in the toroidal direction, which in turn causes further decrease in a (pinch effect). If an inhomogeneity would cause the plasma to kink, $\boldsymbol{B_\theta}$ would be higher on the concave side of the column (right side of kink instability in fig. 2.2) than on the convex one. This effect would then also be self-perpetuating. It was observed that the main driver for the kink instability is often times the bootstrap-current (j_{BS}, parallel current in the plasma edge region) and not the externally driven plasma current as previously thought.[34]

Both types can be suppressed relatively well with a high enough toroidal magnetic field, as its field lines would counteract the resulting field line tension. However, both instabilities are of significance when it comes to the upper boundary of the tolerable plasma current. The kink instability is of relevance when it comes to ELM analysis, because they are the
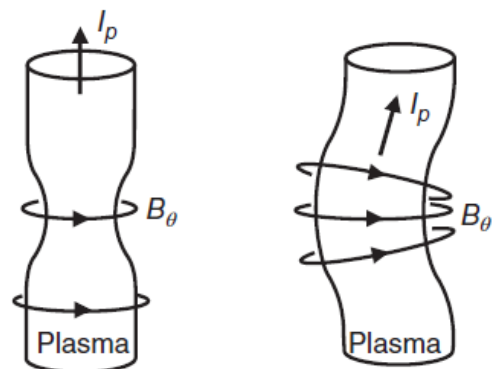

Figure 2.2: An illustration of the sausage (left) and kink (right) instability, both are current driven. Adapted from [27]

precursor of the peeling instability. These arise from large bootstrap flows located in regions

of large pressure gradients, which in turn prevail at the plasma edge. As these kink instabilities gain in radial width, they "peel off" the outer flux tubes and henceforth expel large amounts of confined plasma. The peeling mode limit is of low toroidal mode number ($n \leq 5$) and broad radial extent.[29, 28]

Pressure Driven Instability

Within the plasma small pressure perturbations can experience serious amplification. This phenomenon is especially pronounced at the plasma edge (due to steep gradients) and can lead to ballooning or interchange instabilities. The second type forms in the presence of forces F acting on charged particles in a magnetic field B. In general, a particle experiencing a force will drift (v_f) perpendicularly to both the field and the force:

$$v_\mathrm{f} = \frac{1}{Q} \frac{F \times B}{B^2} \tag{2.2}$$

If the force is dependent on charge (Q), both electrons and ions drift in the same direction. In contrast to charge independent forces (such as e.g. centrifugal or gravity), which causes electrons and ions to move in opposite directions forming an electric field E, which in turn causes an $E \times B$-drift. This drift can lead to an exchange between plasmas of different flux tubes (hence the name interchange instability). A similar phenomenon in fluid dynamics occurs when a heavy liquid is suspended by a light one (Raleigh-Taylor instabilities).

Interchange instabilities exist in tokamaks due to their geometry which creates an curvature drift. The drift underlying force is charge independent and therefore forms a vertical E concentrated at the boundary of areas of different density.. Depending on which side of the tokamak you look at (viewed from magnetic axis), the $E \times B$-drift either enhances or diminishes pressure-driven instabilities. With both gradient and curvature in parallel configuration, the inside of the torus stabilises ∇p-driven perturbations. Whereas on the outside, those perturbations are intensified. Therefore, the inside is said to have good curvature while the outside has a bad one (see fig. 2.3).
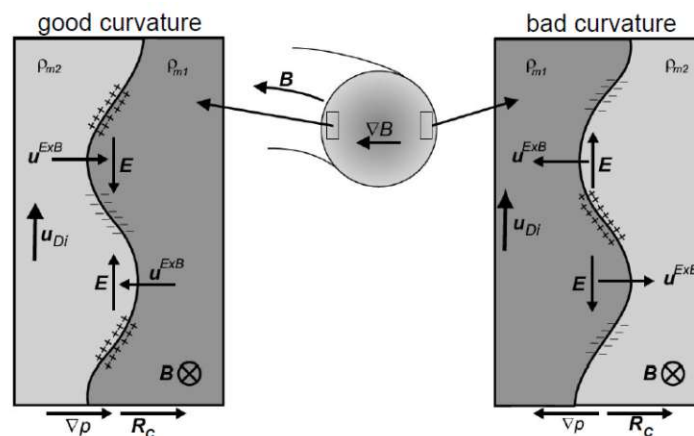
Figure 2.3: Illustration of interchange instabilities in a tokamak. With the pressure gradient ∇p always pointing radially inward (with respect to the minor radius) and the centrifugal force outwards (with respect to the major radius), a region of good curvature persists on the inner side of the torus and a bad one on the outside. Adapted from [31].

Up to a certain pressure, the usual cycle of an interchange instability mode occurring after formation is that it is suppressed on the path along the field lines, since the region of

good curvature has a stronger influence. This is due to the $1/R$-decay (R being the major radius of the torus) of the toroidal B-field with the small R weighting of the inside (being stronger than the larger one from the outside). However, at higher pressures, the stabilizing effects cannot attenuate the instability anymore and the mode expands the plasma on the bad curvature side similar to a balloon (therefore ballooning instability).

Two key parameters in determining ballooning stability are the normalised pressure gradient (α) and the magnetic shear (s). Latter is a measure of the radial variation in the magnetic field line's poloidal inclination. Through numerical testing of the ballooning equation, it can be determined for which α and s values a stable solutions exists.[29] These ballooning stability parameters are defined as follows:

$$\alpha = -\frac{q^2 R}{\boldsymbol{B_\phi}^2/(2\mu_0)}\frac{\mathrm{d}p}{\mathrm{d}r} \tag{2.3}$$

and

$$s = \frac{r}{q}\frac{\mathrm{d}q}{\mathrm{d}r}. \tag{2.4}$$

The safety factor $q = \Delta\phi/\Delta\theta$ (not to mistake with charge Q) defines the helicity of a magnetic field line as change of toroidal angle ϕ per poloidal angle θ, $\boldsymbol{B_\phi}$ the toroidal field and r the poloidal plasma radius. In order to eliminate radial coupling of the modes and therefore assess the situation for each flux surface only perturbations of high toroidal mode number ($n \to \infty$, opposite to the current driven instabilities which have low n) are considered.

After a successful stability analysis for a range of values, the results are plotted into a s-α-diagram. Figure 2.4 shows the stability boundary for a tokamak with large aspect ratio and circular flux surfaces. There are two regions of stability, with the first one being bound by the pressure gradient that the magnetic shear is able to sustain. The existence of a second region was not assumed a priori, but due to the Shafranov shift, even high pressure gradients are allowed at small s. This phenomenon is the result of the hoop force and plasma pressure and it causes displacement of the inner flux surfaces radially outwards. As a result, the field lines on the low field side become steeper, which in turn shortens the distance and time field lines spend in the region of bad curvature. This causes local variations along the flux surface (s can even become negative) creating a magnetic well suppressing emerging instabilities, while the surface-average s remains small. It is due to both, the Shafranov shift and the edge bootstrap current, that the second region of stability is accessible. The influence can be observed in fig. 2.4 by the shift from the red to the blue area.

Figure 2.4: s-α stability diagram with indicated stability regions for a tokamak with large aspect ratio and circular flux surfaces. The second region becomes accessible due the inclusion of the Shafranov shift and edge bootstrap current. Adapted from [29].

Although ballooning modes enhance the transport locally, it is the condition that the pedestal range is becoming unstable to coupled peeling-ballooning modes that triggers an ELM-crash. Within the scope of this work, the plasma was investigated towards ballooning and PB stability. The approach in analysing the plasma ballooning stability (further ex-
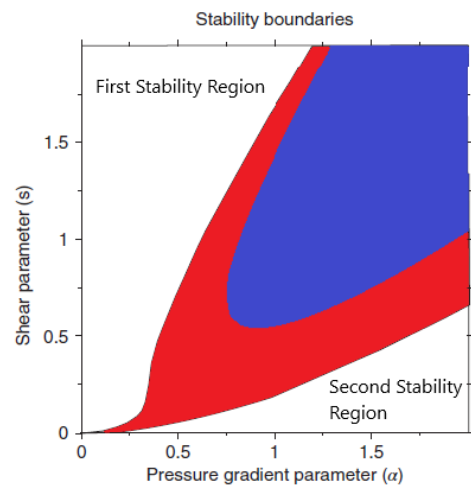
plained in section 5.2) consists of determining the local stability for $n \to \infty$ via the code HELENA.

ELM Triggering Mechanism

As the plasma is heated (currently via external sources), the edge pressure gradient evolves and reaches a critical value α_{crit}. According to the peeling mode limit the plasma will become ballooning unstable and consequently expel particles and energy. However, discharges with α above the critical pressure gradient were observed, meaning that another factor must be involved in the formation of ELMs.[35] The collisionality (ν^*) dictates the magnitude of the bootstrap current in the plasma edge. As can be seen in fig. 2.5, depending on its value the plasma tends to be more ballooning unstable (high ν^*) or peeling unstable (low ν^*).
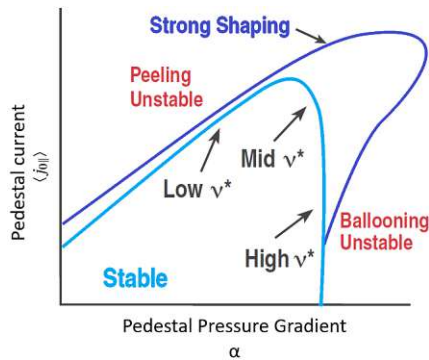

Figure 2.5: Diagram of the PB stability boundary with the denoted effect of ν^* and influence of plasma shaping. Adapted from [36]

In the case of low ν^* the current instabilities can build up without stabilizing effects in contrast to high ν^* which suppresses their growth. The figure also shows the positive effect of plasma shaping on the PB stability boundary. These current and pressure-driven instabilities are the basis of the PB theory which tries to describe the operational boundary of the plasma with respect to the edge pressure gradient and $j_{0\parallel}$. It is one part of the current EPED model, which aims to predict the pedestal height and width (radial extent of edge barrier region) prior to the experiment and therefore forecast the onset of ELMs.[36] The EPED1.6 model applies two constraints in developing a prediction for the pedestal characteristics before the experiment.[37] One part is the PB mode limit and the second is given by kinetic ballooning modes (KBM).

Current methods for assessing the PB stability boundary require an equilibrium which is in general reconstructed with data collected during the experiment. The EPED1.6 derives its PB stability boundary in advance via calculations of the MHD code ELITE. This code takes model equilibria, which are characterised by a small set of scalar parameters, and the pedestal width (Δ_{ψ_N} being the pedestal width in normalised poloidal flux) as input. It then calculates the growth rate of several modes ($n \in \{5, 6, 8, 10, 15, 20 \& 30\}$) at multiple pedestal heights (β_{Nped} being the Troyon normalised pedestal pressure) until the growth rate threshold value of the diamagnetic stabilization
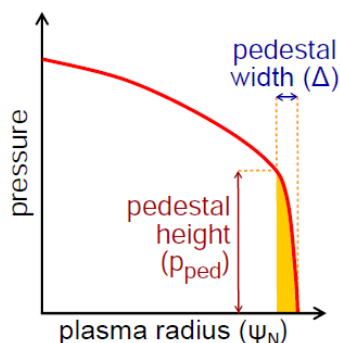
Figure 2.6: Illustration of plasma pedestal height and width in pressure profile over flux normalised radius. Adapted from [30]

model is exceeded. This generates a function of β_{Nped} on Δ_{ψ_N}. Prior studies described a relationship of $\beta_{Nped} \sim \Delta_{\psi_N}^{3/4}$, dictating a less than linear increase with the pedestal width and hence a maximum pedestal gradient.

The second constraint regarding KBM is based upon the limit of local gradient growth as they are the kinetic version of local MHD ballooning modes and hence also become destabilised as a certain pressure gradient is reached. In order to generate the KBM constraint EPED1.6 utilises the "BCP" technique. The scheme is based upon taking the same equilibria used in the PB constraint analysis and increasing the pedestal height at a fixed width until the profile reaches or surpasses criticality across the cen-

tral half of the ETB. This process is repeated for $\Delta_{\Psi N} \in \{0.03, 0.04, ..., 0.08\}$ and the derived data points are then fitted to generate the KBM constraint boundary. The resulting fit shows a relationship of $\Delta_{\Psi N} = \beta_{p,ped}^{1/2} G(\nu^*, \epsilon, ..)$ where $\beta_{p,ped}$ is the pedestal top normalised pressure, G is a slightly fluctuating function of collisionality and aspect ratio (ϵ) and other dimensionless parameters ranging inbetween values of 0.07-0.1. For inputs to the equilibria typical of four tokamaks (AUG, DIII-D, JET & ITER) $\langle G \rangle$ has a value of 0.084 ± 0.010.

The combination of both constraints allows for a prediction of the pedestal width and height. The EPED model dictates that as the plasma transitions to H-mode, its initial pedestal width given by the ETB will widen until it reaches the KBM limitation (dotted line in fig. 2.7). The combination of both constraints allows for a prediction of the pedestal width and height. Subsequently, the operational point will follow the curve to the right by increasing the pedestal top pressure. During the pedestal height increase, α is believed to be fixed at a KBM onset value.[37] The pedestal widening comes to a hold as the PB constraint is reached (denoted with the diamond in fig. 2.7) and the plasma will then linger at this point or run through an ELM cycle.

Within the EPED model and non-linear MHD simulations of type-I ELMs, an ELM event is described in the following sequence:

Figure 2.7: Pedestal height and width prediction of EPED1.6 model of DIII-D discharge 132003 (denoted with black diamond). The dotted line represents the KBM constraint and the solid blue line is the PB constraint. The DIII-D measurement on discharge 132003 is indicated with a red square with its 15% measurement uncertainty. The ELM cycle is denoted by the purple, gray and dark gray curves. Adapted from [37]

Initially, the magnetic field lines start to ergodise as the precursor mode reaches criticality.[38] The connection of flux surfaces of different temperatures causes rapid diffusive parallel heat transport which in turn leads to a pedestal top pressure loss due to a flattened pressure gradient. It was observed that the radial electric field degrades faster than ∇p, which counters the stabilizing effect of the decrease in bootstrap current and ∇p and in turn promotes explosive growth of PB modes. Another effect of PB instability could be the localised increase of ∇p via precursor modes, pushing the plasma towards instability. The pressure gradient subsidence is followed by a shrinking of the pedestal width (indicated by the purple line in fig. 2.7).

After the ELM crash, the pressure gradient recovers and the pedestal pressure is able to build up again until it reaches the KBM limit (indicated by the gray line), where the maximum allowed gradient widens the pedestal (indicated by the black line). The EPED1.6 predictions seem to agree well with measurements (measurement uncertainty of 15% for DIII-D and ∼ 15% at JT-60U, JET & AUG) and hence present a good tool for edge stability analysis prior to a plasma discharge.[37]

The PB stability analysis workflow at ASDEX Upgrade utilises calculations of the code MISHKA (further explained in section 5.2), which follows the EPED model by applying the KBM constraint ($\Delta_{\Psi N} \propto \beta_{p,ped}^{1/2}$.)[39]
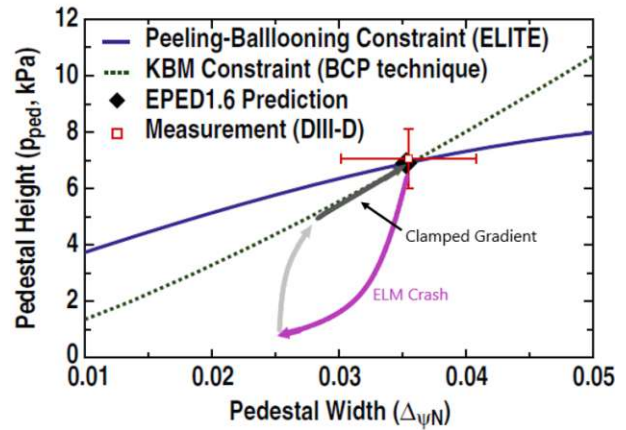
2.2   Power Exhaust SOL Mitigation Mechanism

The general description of the power exhaust mitigation mechanism and certain phenomena throughout this section are based on the following publications [26, 27, 31].

For current ITER and DEMO operation a heat load in the order of several 100 MW/m^{-2} and therefore beyond the designated 10 MW/m^{-2} is estimated.[40, 19] The undamped particle and power exhaust in steady state operation would severely damage the divertor tiles and subsequently make the machine inoperable. To counteract the degradation, the divertor region geometry was hence modified so that two exhaust-reducing mechanisms (radiation and volumetric processes) could be capitalised to its fullest.[31]
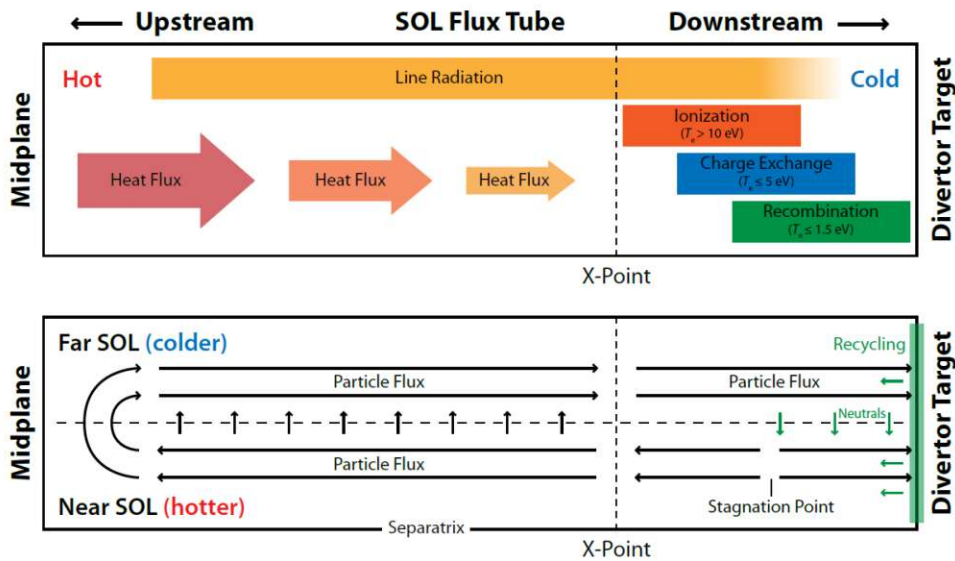

Figure 2.8: Illustration of energy and particle flow in the SOL. The top part shows the heat flux travelling from the midplane to the divertor with the major volumetric processes denoted. The lower part describes the main ion particle flux patterns. Adapted from [41].

2.2.1   Radiation Losses

One part of the optimization was to enhance the energy loss through radiation. The upper part of fig. 2.8 shows the heat and particle flux in the SOL from the midplane to the targets. The highest temperature in the SOL exists at the midplane and the lowest one in the divertor region.[41] This results in a parallel (to the magnetic field lines) temperature gradient and therefore transport from the midplane (also called upstream) to the divertor (also called downstream) . The non-fully ionised particles emit electromagnetic energy in form of line radiation as they travel along the field lines.[27] Depending on the impurity concentration and species, and the prevailing radiation efficiency (see section 2.2.3), line radiation is dominant form of power loss in the high temperature SOL region and varies in intensity by atomic species. Therefore, increasing the time that particles spend in the SOL was a decisive factor in the optimization.[31]

2.2.2   Volumetric Processes

Secondly, the focus was directed towards a high neutral gas pressure in the divertor area. The neutrals reduce their momentum and interact with the incoming particles through vol-

umetric processes. These include ionization, charge-exchange and recombination. Each of them has an individual temperature dependent cross-section; therefore they all dominate in different areas in the SOL. If temperatures reach around 10 eV in the divertor, the power flux loss through ionizing neutrals starts to gain in intensity. Energy dissipation through charge-exchange becomes significant at around 5 eV and through recombination below 1.5 eV. As a result of these processes, the power flux particles become neutral and can therefore carry away momentum by leaving the plasma.

2.2.3 Impurity Radiation

Due to sputtering (see section 2.3.1), the core plasma can become unintentionally contaminated with a small share of non-fuel particles. These medium- to high-Z particles (e.g. Be, C, W, ...) can in some instances pose a problem to the continuous plasma operation because they have the ability to cool the plasma severely leading to a lower fusion rate, confinement degradation, or in the worst case disruption. The cooling is the result of the significantly higher radiation efficiency of these impurities than hydrogen, therefore expelling energy faster than can be supplied externally (through plasma heating) or internally (through α-particle heating). Figure 2.9 shows the cooling factor L_z (also radiation efficiency factor) of several elements as a function of temperature.
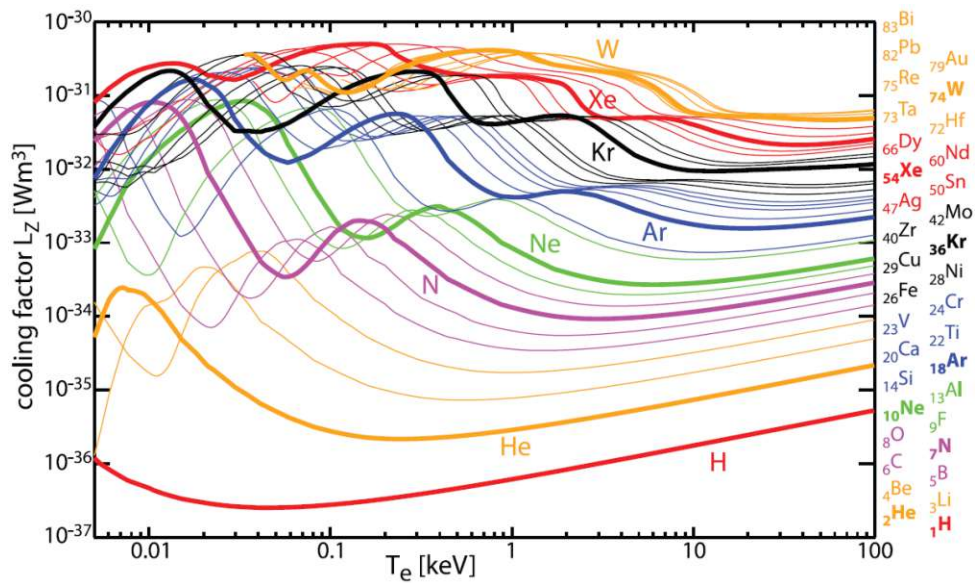
Figure 2.9: Temperature dependence of the cooling factor for several elements at $n_e = 5 \times 10^{19}\,\mathrm{m}^3$. Adapted from [42].

L_z is the normalised radiation loss rate $P_{\mathrm{rad,z}}$ of an element. It serves as a parameter to compare the radiated power of different species at equal particle concentration c_z, electron density and temperature.

$$P_{\mathrm{rad,z}} = L_z \cdot n_e \cdot \underbrace{(c_z \cdot n_e)}_{\text{impurity share}} = L_z \cdot \frac{p_e}{T_e} \cdot (c_z \cdot n_e) \tag{2.5}$$

To calculate L_z, the individual rate coefficients for ionization, recombination and line excitation are used in a collisional-radiative model and summed up.[43] For heavier elements

these calculations are very complex, due to their electronic structure. That is why some assumptions and limitations exist to these values.[42]

It is also crucial to consider how long the particle stays in a given temperature region. If the ionization stages of the element can reach an equilibrium at the given plasma electron density and temperature, it has reached coronal equilibrium.[44] In an instance where the transport is faster than the required residence time τ, this situation is referred to be in a non-coronal equilibrium. This holds true to the divertor and to the pedestal region with the presence of ELMs where τ can be below 1 millisecond.[43] To factor this in, the impurity residence time is taken into account when calculating L_z. The effect is pronounced during the ionization to the equilibrium charge state and its mechanisms are documented in [45]. As fig. 2.10 indicates, the radiation efficiency enhances when a non-coronal equilibrium is included.

To summarise the process of accurately estimating the precise radiation efficiency value is a complex task. However, in fig. 2.9 it can be observed that for temperatures above 1 keV (which are present in the confined plasma) in general the higher the atomic number the higher L_z is. This circumstance can be attributed to the fact that particles being fully stripped of their electrons (a state that requires more energy the higher the Z number) solely emit low residual levels of bremsstrahlung.[26]
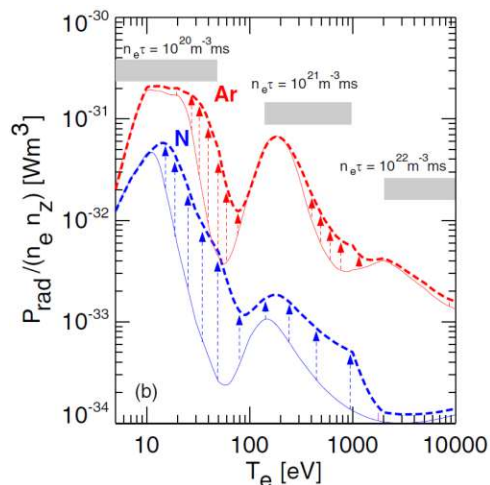

Figure 2.10: The effect of non-coronal equilibrium (dashed line) on L_z with adequate $n_e\tau$ values for the divertor and pedestal region. The grey horizontal bars display regions of constant non equilibrium parameters and the chosen estimated value. Between the grey bars a linear interpolation was used. Solid lines represent the equilibrium L_z. Adapted from [43].

The outcome of the L_z analysis is that these high-Z particles pose a serious threat if they accumulate in the core. Due to their high radiation efficiency they cause the core plasma to lose its high temperature and consequently lead to the problems that were mentioned at the subsection's beginning. Early studies found that in order to have less than 50% of the α heating emitted as radiation by the impurities (thereby still allowing for ignition), the maximum impurity level for high-Z atomic species as tungsten may not surpass concentrations of $\sim 10^{-5}$ per hydrogen ion.[46] Recent studies demonstrate through the development of different models and usage of the transport code ASTRA that the maximum impurity concentration heavily depends on the He confinement time and that it inversely scales with the impurity's atomic number squared ($\approx 1/Z^2$) leading to a maximum tolerable concentration of for example tungsten from $10^{-3} - 10^{-5}$.[42] However, contrary to sputtering, the mean of deliberate seeding of impurities has shown to have a positive effect on the plasma behavior and target conditions (see section 2.3.5).

2.3 Divertor Region

The general description of the divertor region and certain phenomena
throughout this section are interpretations of the following publications [26, 27, 31, 46].

ITER and DEMO will work with a divertor configuration, which means that energy and particles are directed towards the divertor region where they strike the tungsten tiles. As in section 1.2 previously mentioned, the main reasons of choosing tungsten as wall material in the divertor region, are its high melting point and good thermal conductivity. Additional benefits are its low atomization and retention of hydrogen isotopes.[31]

Only a relatively small area of the targets is utilised as plasma-wetted surface which results in a high load for the target. Due to that, multiple material degradation processes occur. The sputtered particles then follow distinct particle flow patterns which are briefly discussed in the coming part. The following section touches on the fundamental target interactions, the resulting flows and prevention of heat overload in the divertor region.

2.3.1 Sputtering

In addition to the obstacles mentioned in the last paragraph of section 2.2.3 , medium- and high-Z matters (originating from wall material or deliberate seeding) cause amplified ablation (in contrast to hydrogen) of the divertor material.[26] They carry higher impact energies as they are accelerated by the pre-sheath and sheath potential. These two potentials are situated over the target area and reach a thickness of about $100\lambda_D$ and $10\lambda_D$ (Debye length) respectively. The pre-sheath is a quasi-neutral region whereas the sheath breaks the neutrality condition. The potentials arise from the difference in velocities of electrons and ions, as the electrons arrive earlier at the divertor plate and therefore charge it negatively.[27]

Consequently, adding to the obstacle of a possible divertor target heat overload, it is necessary to prevent excessive sputtering of the divertor tiles to avoid substantial plasma energy loss. Analyses of several core impurity concentrations suggested that in order to keep the erosion thickness below 5 mm per two burn years at a heat flux of 5 MW/m^2, a divertor region temperature limit of 5 eV must be kept.[43]

2.3.2 Recycling

As fig. 2.8 shows, the particle flux reduces through volumetric processes on its way to the target plates. The remaining ions are accelerated beyond their Debye length onto the wall surface where they can acquire neutral state and as such become part of the surface material by co-deposition or diffusion - or they bounce off the wall. The reflection process is called recycling and applies to almost all of the wall interactions as the divertor tiles become saturated with main fuel particles.[31] Reflected neutrals then can either remain in the vessel and potentially make their way back into the confined region or be removed from the vessel through cryopumps.

2.3.3 Power Exhaust Counter-Current Flow

Figure 2.8 also illustrates the path neutrals can take following the reflection off the target. As they move towards the incoming particle exhaust they re-ionise which, depending on the upstream location of this event, predominantly forms either a flow back to the divertor or further up. The stagnation point marks the position to which extent the region (where ions

mainly create a concurrent power exhaust flow) expands up to from the target. Particles further upstream form a counter-current to the plasma exhaust. The area in close proximity of the stagnation point acts similar to a "watershed".[46] The flow away from the target is caused by poloidal and/or toroidal drifts, as well as an ionization-driven flow. The latter is caused by the temperature distribution in the divertor. With the separatrix being the hottest part of the plasma leg (the magnetic field lines in the SOL connecting to the divertor), it promotes ionization more than the outer flux tubes which are situated in the SOL and the private flux region (the volume enclosed by the plasma legs in the divertor region). This generates a stronger ion source in the near-separatrix region. To level the particle-imbalance, the previously mentioned reversed ionization-driven flow develops.

The counter-current diminishes before reaching the midplane via diffusive radial transport. The stagnation point in the high recycling regime (a regime that features a recycling flux that is proportional to n_e^2) sits between the targets and the X-point.[41]

2.3.4 Divertor Detachment

In high performance discharges of medium sized devices the divertor is in an attached state, meaning that the conditions downstream at the targets are connected to the upstream values and the exiting power flux. This implies that without measures sufficiently reducing the parallel heat flux in the SOL from the midplane to the target, the target surface temperature would exceed tolerable values. In order to quantify the relationship between up- and downstream conditions, the so-called two-point model is employed. This model is based on the assumption that the SOL power flux from the upstream position to the recycling zone is solely carried by parallel electron heat conduction without power in- or outflow (e.g. due to radiation or volumetric processes). The resulting equations describing the downstream conditions provide an estimate of the necessary upstream and heating power conditions for achieving a significantly lower downstream than upstream temperature. It can be shown that a certain upstream density has to be reached (which is dependent on the plasma heating power) to have a manageable target temperature.[31]

Conditions in discharges at several tokamaks have been achieved, where the divertor plasma pressure over the whole target is lower than the upstream value.[47] This detached state has been reached due to power flux mitigation measures. It is the aspired divertor regime during operation, as it prevents thermal overload and excessive sputtering.
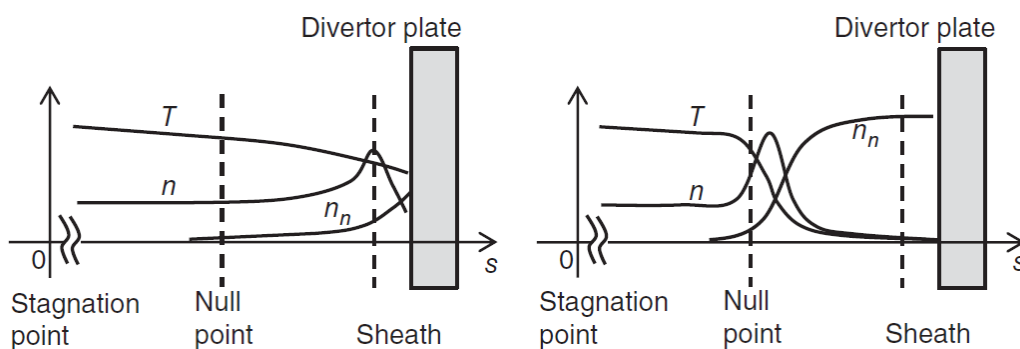

Figure 2.11: Course of the plasma temperature (T) and density (n) and the neutral density (n_n) in the divertor region in attached (left) and detached state (right). The null point denotes the location where the poloidal field is zero, called X-point within this thesis. Adapted from [27].

Through additional gas fuelling in the divertor the neutral density rises and a transition

into the high recycling regime occurs. This initially promotes a reduction in temperature to sustain constant plasma pressure and as these conditions cause less particles to become fully-ionised (which subsequently elevates their radiation efficiency), the temperature decreases even further. From this follows less sputtering as the sheath thickness shortens ($\lambda_{\mathrm{D}} = \sqrt{\epsilon_0 T_{\mathrm{e}}/(n_{\mathrm{e}} e^2)}$).[46] The higher density also mitigates the power exhaust by decreasing the particle flux momentum via friction and charge-exchange (requires $T < 5$ eV). The divertor is said to approach a state called partial detachment, characterised by a pressure drop near the separatrix along the target. The issue of an excessive power load remains as the ions deposit their recombination energy on the tiles. However, if the temperature allows for recombination reactions (requires $T < 1$ eV) the divertor is said to be in full detachment and the pressure over the whole divertor surface drops.[31, 27]

If the radiation losses can be enhanced by measures of impurity seeding, the divertor region is sufficiently cooled and its attachment to the SOL is further reduced. The divertor plasma gradually starts to detach from the tiles, and n_{e} and T_{e} along the target become independent of the upstream conditions. Finally a front of neutral gas forms in front of the target plates resulting in a fully detached divertor.[26]

This transition is depicted in fig. 2.11) with the left subplot showcasing attached divertor conditions and the right part detached divertor conditions. The figure illustrates the condition in which radiation losses after the null point are enhanced, therefore cooling the plasma in this vicinity and causing an upstream shift of the ionization front and hence plasma density peak. The neutrals consequently move further upstream (up to the temperature drop) as they encounter lower temperatures and conditions that promote recombination.

During the transition from attached to fully detached, the divertor region experiences different grades of detachment. Their respective heat flux distributions are shown in fig. 2.12 further highlighting the tremendous effect and significance of full detachment. A measure of assessing the grade of detachment at ASDEX Upgrade is to observe the edge current. This current forms because of thermoelectric effects, by Pfirsch-Schlüter currents.[49] The thermoelectric current originates from the difference in Debye sheaths (originating from the different electron temperatures) of the inner and outer target.[50] Due to its dependence on the temperature difference, it is possible to derive the target temperatures from the measured current and therefore make an assumption about the state of detachment.[26] See section 3.4 for further information.
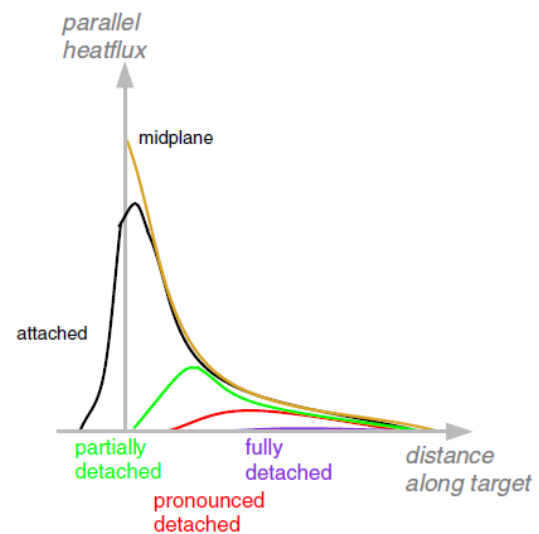

Figure 2.12: Different states of detachment and their respective power load profile on the outer divertor target. Adapted from [48].

2.3.5 Divertor Impurity Seeding

The existing line radiation and volumetric processes do mitigate the heat and particle flux, but not to the required safe-for-operation levels in future devices. At the ASDEX Upgrade

tokamak a method was developed to prevent a divertor heat overload: The deliberate introduction of low- to medium-Z impurities into the device to dissipate the power flux's energy.[43]
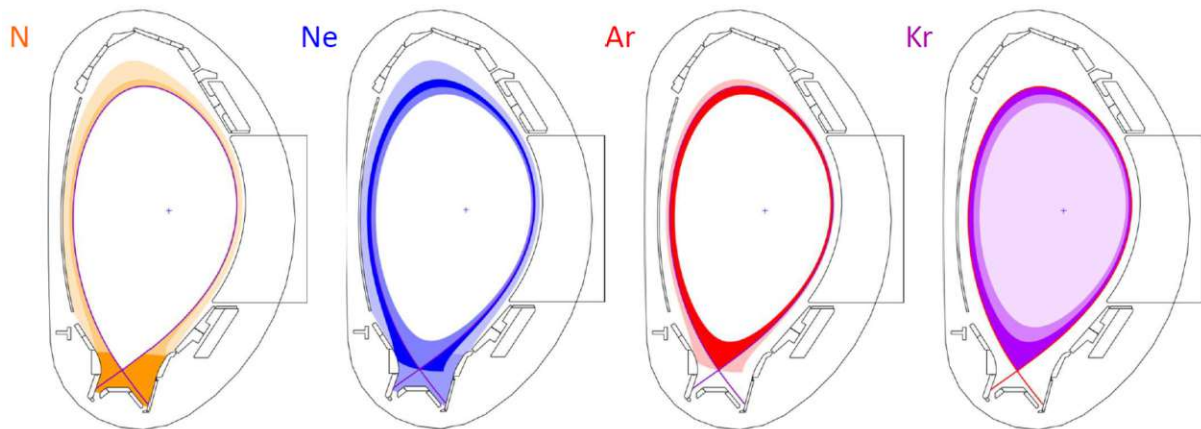

Figure 2.13: Radiation intensity distribution of different low- to medium-Z impurities. Adapted from [51].

However, in order to avoid plasma disruptions, the seeded impurities must be well retained in the divertor region and should not induce strong core radiation. These requirements are met by low- to medium-Z impurities as they are fully ionised before reaching the confined region leading to a reduction in L_z. Figure 2.13 displays the distribution of radiation intensity for different impurity species and fig. 2.14 their radiation efficiency for divertor relevant temperatures.
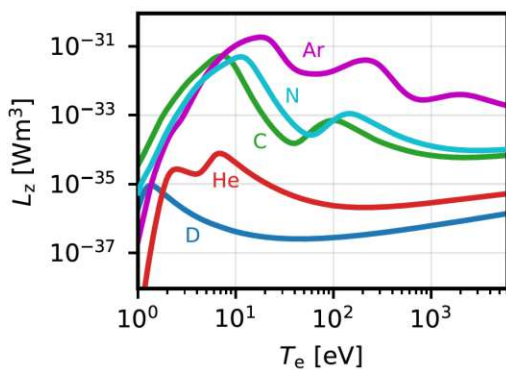

Figure 2.14: "Radiation efficiency of different atomic species in coronal equilibrium at $n_e = 10^{19}m^{-3}$ according to the ADAS database [52]."[41] Adapted from [41].

The benefits of choosing nitrogen as a divertor seeding impurity above argon or krypton can be observed in these two pictures, as it offers a sufficiently high L_z in the temperature range needed for safe operation of the divertor and several magnitudes lower L_z compared to argon or krypton for confined plasma temperatures, causing less heat to be radiated in the region of high fusion yields. Figure 2.14's (in contrast to fig. 2.9) temperature range covers that of values that are found in the divertor region, giving a more precise insight into nitrogen's benefits over other atomic species.

However, these other elements provide different advantages that are of interest when it comes to cooling regions in the confined plasma. Neon and Argon prove to be formidable SOL radiators, whilst Argon's L_z is also high in pedestal conditions. As a core radiator, Krypton could be utilised for future machines as it will require dissipation of the immense fusion power that will be generated before it reaches the SOL.

Within the scope of this work only discharges using nitrogen to induce an X-point radiator were analysed.

2.4 The X-Point Radiator

Through the deliberate and controlled seeding of medium-Z impurities at ASDEX-Upgrade and other tokamaks, the formation of a small, poloidally localised radiating volume situated above the X-point and inside the confined region in H-Mode plasmas was observed.[25]

2.4.1 Formation Mechanism of X-Point Radiator

A model for the formation of the X-point radiator was developed in [53]. It is based upon the balance between power entering the X-point region through parallel heat conduction ($q_\parallel$) and power loss due to volumetric processes and radiation, and the boundary condition that it must form at temperatures above the impurities' radiation efficiency maximum. The boundary condition is of importance when it comes to the XPR triggering mechanism.

The power $q_\parallel$ entering the XPR volume ($P_{\mathrm{cond,e}}$) through the effective poloidal XPR area (A_θ) is estimated as follows:

$$P_{\mathrm{cond,e}} = A_\theta q_\parallel \approx A_\theta \hat{\kappa}_{\mathrm{e}} \left(T_{\mathrm{e,u}} - T_{\mathrm{X}} \right). \tag{2.6}$$

Since the heat conduction is mainly carried by the electrons (due to their 60 times higher conductivity in comparison to ions), the power flux can be derived through the electron fluid heat conductivity ($\hat{\kappa}_{\mathrm{e}}$) and the electron temperature difference at the upstream position ($T_{\mathrm{e,u}}$) and the one present in the X-point volume (T_{X}). Also, electrons and ions are said to be coupled in the X-point region, as a high ion temperature would be passed on to the colder electrons almost instantaneously due to the high electron-ion energy transfer.

This conducted power must then be dissipated via the mechanism presented in section 2.2 as radial transport is negligible, in order to have a stable scenario. The key factors in the power balance and their respective temperature-dependence are displayed in fig. 2.15 for a core nitrogen concentration of 1%. The figure shows the increase in heat conduction (red) with T_{X} decrease and the gradual loss of intensity in volumetric processes, up to the region (10-20 eV) where enhanced radiation loss is the dominant power loss driver.

In the shown scenario the XPR region starts with no heat conduction (due to the missing temperature gradient $T_{\mathrm{X}} = T_{\mathrm{e,u}} = 100$ eV), but with a non-negligible power loss through charge-exchange reactions and ionization. This continues until a stable solution at $T_{\mathrm{X}} \sim 80$ eV is achieved where the heat conduction and losses balance each other. In this situation, the X-point region is not able to cool down any

Figure 2.15: The power loss mechanisms' and heat conduction's magnitude in dependence of the XPR volume temperature. Adapted from [53]

further as it would increase ∇T and hence more heat flux into the region. This solution is therefore not allowing the formation of an XPR phenomenon.

The other solutions are located at $1 - 20$ eV, where nitrogen radiation losses are the dominant energy sink. The solution at ~20 eV is unstable as a finite temperature variation would cause the plasma to shift towards one of two other solutions (denoted as **h**igh-**t**emperature
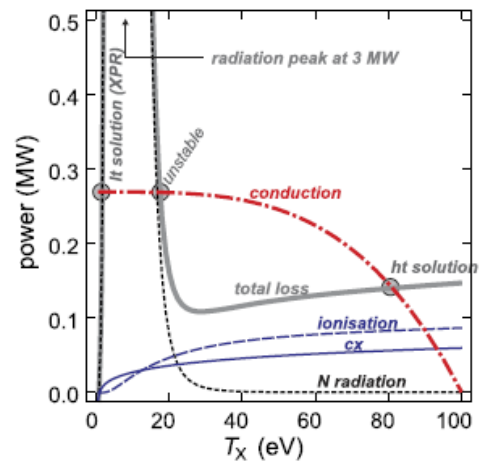
or **l**ow-**t**emperature solution in fig. 2.15). In the case of a small temperature decline, the X-point region would experience a self-perpetuating cooling process until it reaches the lt-solution corresponding to the XPR phenomenon. This process is known as radiation condensation and relies on the physics of nitrogen's negative L_z slope at temperatures around 20 eV. As energy is radiated away, the temperature of the surrounding plasma decreases. Due to L_z's negative slope, this means a higher radiation efficiency - subsequently more energy is being emitted and the temperature drops further. This cycle is also responsible for the emergence of a phenomenon called Marfe.[54] Marfes form at the edge of tokamak plasmas and are a toroidally symmetric high-density radiating band and because they act as powerful energy sinks, they are focus of current research as they pose the risk of plasma disruptions.[53]

The initial power loss cannot be contributed to nitrogen as its radiation efficiency does not contribute significantly to the power loss above temperatures of 20 eV. Therefore, it can be concluded that neutral deuterium plays a significant part in the beginning of the transition from the ht- to the lt-solution. Within the work of [53], it could be shown that for a neutral deuterium density of $3 \times 10^{17} \mathrm{m}^{-3}$, the X-point region cools beyond the nitrogen radiation peak bypassing the ht-solution and only allowing the lt-solution.

A parameter on the lt-solution access (X_A) is derived in [53] via the simplified forms of heat conduction, ionization and charge-exchange reactions, and the usage of the two-point model. The influence of nitrogen is neglected because of its low contribution of line radiation to the power loss above 20 eV.

$$X_A \sim \frac{R_0^2 q_s^2 f_{\exp}}{a} \frac{n_0 n_u}{T_u^{5/2}} \sim R_0^2 q_s^{8/9} f_{\exp} n_0 n_u^{14/9} P_{\mathrm{sep}}^{-10/9} \tag{2.7}$$

R_0 being the major radius, a the minor radius, q_s the safety factor, the flux expansion $f_{\exp}$, neutral and upstream density n_0 and n_u and the net power leaving the confined region P_{sep}. It was derived that in the instance of X_A being above 1, the conditions for an XPR are met. The flux expansion is a measure for the ratio of the radial distance between the nested flux tubes at a certain location in comparison to the midplane values. The fact that the XPR appears at the X-point vicinity is promoted due to the region's high $f_{\exp}$ (see fig. 2.17). Other XPR promoting parameters are high values in safety factor, aspect ratio (R_0/a), upstream and neutral density, whereas heating power or high midplane edge temperature has a hampering effect. An external trigger during operation of the XPR formation could be a decrease of the supplied heating power (hence less power is leaving the confined region) or an increase in the neutral density.

Figure 2.16a shows that in the situation of the full power balance, X_A must exceed a value of 2.3 for an XPR development. A possible transition mechanism from ht- to lt-solution was proposed via the ramp-up of neutral density (black dashed line in fig. 2.16a) until the XPR emerges with a possible ramp-down (indicated with the gray dashed line) to the inaccessible lt-solution. The gray indicated lt-solution would allow frequent flush of impurities through MHD events such as ELMs, which in turn could generate a transition back to the ht-solution or a back and forth between lt- and ht-solution (indicated in fig. 2.16a).[55]

As previously mentioned the influence of the impurity species in the derivation in X_A was disregarded as it does not provide a notable power loss in the higher temperature region. However, it is of importance once the ht-solution is surpassed to provoke thermal collapse ($T_X \sim 1$ eV) and hence the lt-solution. This T_X progression has been shown in nitrogen-seeding induced detachment experiments [56] carried out at AUG. The characteristic T_X development was observed which includes a slow approach towards the ht-solution temperature and a rapid temperature drop to the lt-solution.
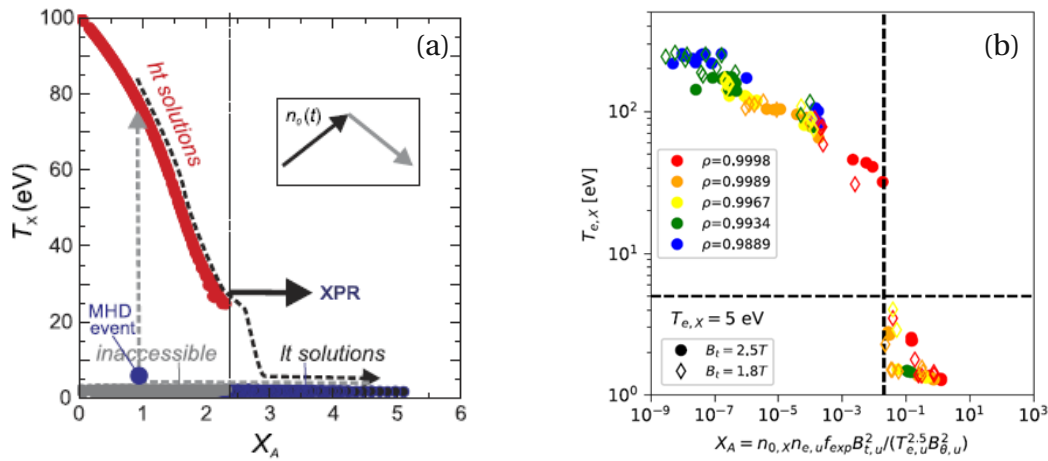
Figure 2.16: (a) Display of the whole power balance solutions and their respective X-point region temperature, concluding a threshold value of $X_A \sim 2.3$. Possible lt-solution triggering mechanisms are shown via means of deliberate increase of neutral density (black dashed line) and subsequent ramp down (gray dashed line) after the XPR has emerged, leading to an operational regime under the inaccessible lt-solution. In addition, MHD events could also allow for operation in the inaccessible lt-solution. Adapted from [53]. (b) XPR access parameter evaluated at different flux surfaces through SOLPS-ITER simulations, confirming the access criteria given in [53] as these regions only experienced XPR-like temperatures of around 5 eV as X_A takes a value above a certain threshold. This analysis was carried out for different toroidal field strengths showing the inward movement of the XPR for higher B_ϕ. Adapted from [57].

Another study looked at the XPR scenario from a 2D perspective and therefore captured source and sink terms present in the X-point region and the occurring transport and drifts that emerge due to high- and low-field side asymmetries. Within the work of [57] it could be shown through simulations of SOLPS-ITER of the XPR, that the access condition parameter does hold true. If the X_A value of a flux tube does reach a certain threshold, its temperature drops to XPR-like values of ~ 5 eV (see fig. 2.16b).

The figure also showcases the effect on XPR develop-ment with regards to flux expansion as more radially inward flux tubes experience lower temperatures at B_ϕ=2.5 T in comparison to B_ϕ=1.8 T. The high toroidal magnetic field appears to push the XPR inside.

The process of XPR development in [57] is induced via seeding of impurities, which serves to cool the di-vertor region. A cycle of line radiation cooling down the vicinity of the X-point further allowing for more line radiation and so forth is initiated. This process is (as previously mentioned) promoted by the large con-nection length and flux expansion in the X-point area which allows for energy loss via volumetric processes within the plasma. The presence of a parallel tem-perature gradient inside the confined region leads to conductive parallel heat flux from the upstream region in a small separatrix layer. Consequently, the SOL re-ceives less heat, causing it to become even more trans-parent for neutrals. As a consequence, more neutrals
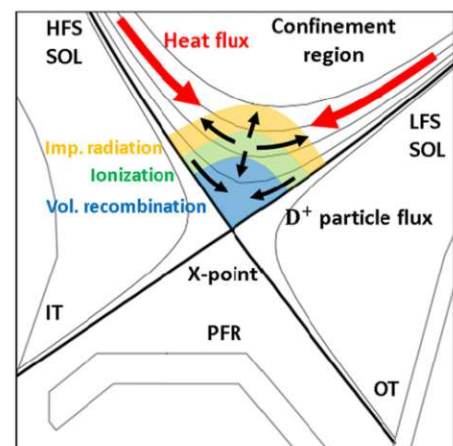

Figure 2.17: Diagram of X-point region with denoted power balance source and sink terms (volumetric processes and their respective dominant region) and drifts. Adapted from [57]

are able to reach the X-point region before getting ionised, increasing both the density and pressure of the plasma. This generates a radially inward diffusion and parallel convective particle flux from the X-point area to the upstream region. As the X-point region cools down further ($T_X \sim 1$ eV) it experiences a substantial increase in volumetric recombination, leading to a considerable drop in plasma pressure. This pressure reduction is primarily driven by volumetric processes, momentum diffusion (resulting from neutrals leaving via charge exchange and recombination), and radial transport. Furthermore, there is a parallel convective particle flux from the ionization to the recombination zone. Although recycling in the divertor reduces, the overall ionization rate remains consistent due to recombination occurring in the X-point region. These mechanisms are showcased in fig. 2.17.

In fig. 2.18 several plasma parameters and processes are displayed stemming from simulations of [57] including drifts. The highly radiating area in subfigure (a) indicates the XPR. Figure 2.18(b) shows that the radiation front occurs in the vicinity of sharp temperature drops (reason being the promoting factors of higher) and that the divertor is in full detachment. Subfigure (c) shows the previously mentioned pressure drop in the XPR area. An ionization band forms around the XPR and in its center a ion sink established by the high amount of volumetric recombination. A plasma potential emerges in the ionization region, creating a radial and poloidal electric field which subsequently generates $\boldsymbol{E} \times \boldsymbol{B}$ drifts. The $\boldsymbol{E}_r \times \boldsymbol{B}$ drift causes a drift from the X-point area to the HFS and the $\boldsymbol{E}_\theta \times \boldsymbol{B}$ drives the particles below the XPR from the HFS to the LFS. These findings agree well with measurements from the divertor TS diagnostic. In addition, the upstream values were also affected by the XPR, as the radial electric field responsible for the stabilizing shear effect shifted inwards causing an inwards shift of the pressure profile as well. It was assumed that this might be a key mechanism in explaining the suppression of ELMs in the XPR operational regime.[57]
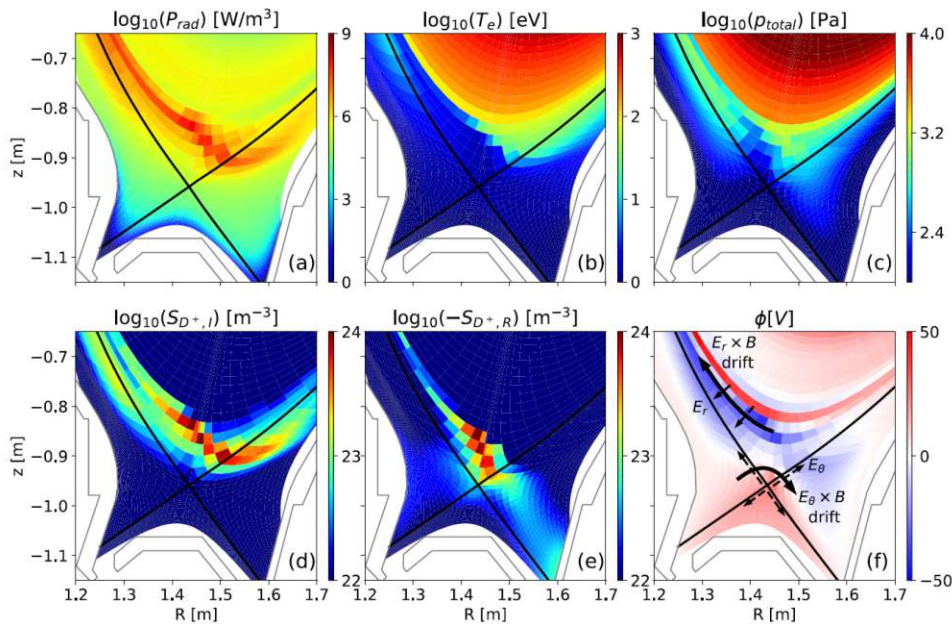

Figure 2.18: 2D simulations including drifts for (a) the radiation density, (b) electron temperature, (c) total pressure, (d) deuterium ionization and recombination (e), and (f) the plasma potential with drifts. Adapted from [57]

An earlier study concluded that the radial electric field differs from the neoclassical expression which as well could possibly explain the ELM suppression.[24] Also the potential peak/valley (depending on $\boldsymbol{B}_\phi$ orientation) was also observed within [24] and explained to

be necessary to drive the Pfirsch-Schlüter currents through the cold and hence highly resistive PFR. Throughout [24], it was also observed that as the divertor detachment enhances the nitrogen is better retained in the divertor area. Additionally, the nitrogen poloidal flow's stagnation point moves farther from the target, thereby enhancing the likelihood of nitrogen returning to the target following recycling and re-ionization. The simulations in [24] also concluded that the maximum radiation location of the XPR moves from the X-point upwards to the outer midplane with higher nitrogen-seeding and heating power which was also observed in experiments.

2.4.2 XPR Control and experimental Observations

Experimental Observations with XPR presence

It has been observed that with an XPR vertical position of 7cm above the X-point, ELMs become suppressed (ELM signature disappears in $I_{polSOLa}$, divertor radiation and/or quasi-periodical reduction of stored energy).[23] The XPR height of ~7 cm (ELM-free access condition) accounts only for a radial width of 2mm when mapped to the midplane further displaying the effects of flux expansion. The divertor reaches full detachment, which subsequently leads to an increase in the neutrals compression and for discharge #36655 at AUG a reduction in core tungsten concentration from 4×10^{-5} to 2.5×10^{-5} was found while simultaneously the core nitrogen concentration was only around 2-2.3%.

A full tomographic reconstruction of discharge #36655 at AUG is presented in fig. 2.19 which visualises the extent of the XPR and its power density. The discharge utilised in this figure is part of the database of this work.

Active XPR controller

The XPR is in contrast to Marfes a stable phenomenon that can be actively controlled and does not lead to an unstable plasma.[25] A real-time controller has been implemented at AUG which uses lines of sights from XUV-cameras to estimate the vertical position of the XPR to the X-point in a range from -10cm (below) to +20 cm (above) at a rate of 20 ms to filter out ELM values.[23] The controller is then programmed to reach and maintain (in the future also countering possible position oscillations) the vertical XPR position to pre-programmed values via means of nitrogen seeding (in the future possibly also via heating). To induce the XPR the discharge is pre-programmed to introduce specific values of N_2 into the tokamak through the PFR up to 3 seconds after which the controller will take over. This measure is necessary to avoid confusion by the real-time controller through the detection of faulty radiation peaks prior to the XPR presence. Stable XPR operation of up to +15 cm above the X-point (equivalent to $\rho \sim 0.985$) has been achieved.
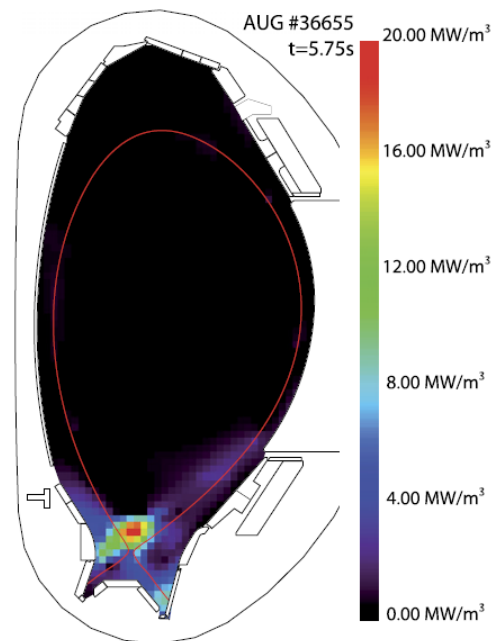

Figure 2.19: Tomographic visualization of the radiated power in discharge #36655 at AUG with the presence of X-point radiator.[23]

To sum up, the X-point radiator can be introduced by strong Deuterium and Nitrogen seeding. In this plasma scenario the divertors are detached and power load to the plasma facing components are mitigated. The physical mechanism that leads to the XPR is well understood and can be modelled with 2D fluid codes taking account of the drifts. Experimentally, the position of the XPR can be controlled, with the soft X-ray cameras as position controller and the N seeding valves as actuator. It has been found that the ELMs disappear at a certain position of the X-point radiator. We know that ballooning modes increase radial transport, but that it is the coupling of peeling-ballooning modes over the extent of the pedestal width that triggers an ELM-crash. In order to understand the ELM behaviour, the edge profiles and their stability against local ballooning and global peeling-ballooning modes will be investigated for different positions of the X-point radiator.

Chapter 3

Diagnostics and advanced Profile Determination

The following part addresses the various diagnostics which were utilised in collecting the experimental data and the integrated data analysis approach in generating the corresponding plasma parameter profiles.

3.1 Charge Exchange Recombination Spectroscopy - CXRS

The Charge Exchange Recombination Spectroscopy (CXRS) is a commonly utilised diagnostic among magnetic fusion devices for measuring ion properties. It is based on the interaction between the impurity ions and the injected neutral atoms distributed through neutral beam injection or gas puff. As the neutral Deuterium (D^0) atoms enter the plasma, they can exchange electrons with the impurity ions (A^{Z+}) and thereby excite them. These impurities then de-excite under the emission of a characteristic photon ($h\nu$). Through the analysis of the emitted spectrum the temperature, density, poloidal and/or toroidal velocity (depending on the orientation of the diagnostic to the plasma), and the electric field can be derived.

$$D^0 + A^{Z+} \rightarrow D^+ + A^{(Z-1)+*} \rightarrow D^+ + A^{(Z-1)+} + h\nu \tag{3.1}$$
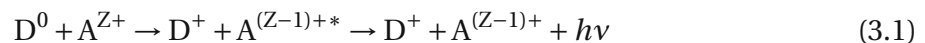
The main two assumptions for the CXRS are that the excited ions have the same energy and velocity as the bulk and that the impurity (T_{imp}) and main ion (T_{i}) temperature are approximately the same as the temperature equilibration time is below the transport time scale.[58]

By evaluating the characteristic line emission, a Gaussian-shaped profile around the characteristic wavelength is observed. This is the result of the Doppler broadening due to the Maxwell-Boltzmann velocity distribution of the ions. Through the assessment of the full width at half maximum (FWHM) of the Gaussian, the temperature can be deduced and the intensity indicates the ion density (n_{i}). Through the installation of poloidally and toroidally orientated optical heads, it is possible to retrieve the respective velocity of the ions (v_{p}, v_{t}).

There are multiple CXRS systems installed at AUG measuring several impurity species (He^{2+}, B^{5+}, C^{6+} and Ne^{10+}) from the high- (HFS) and low-field side (LFS) of the tokamak probing the core and edge plasma region. Each one is equipped with a high-throughput Czerny-Turner spectrometer with charge-coupled device (CCD) cameras. The high spatial and temporal resolution (2.3 ms core CXRS, 10 μs for edge CXRS which has a modified sys-

tem with an electron multiplying CCD camera allowing for ELM study), offers a detailed ion property measurement to the extent of a poloidal asymmetry analysis.[59, 60, 61]

3.2 Deuterium Cyanide Laser Interferometry - DCN

The Deuterium Cyanide Laser Interferometry (DCN) diagnostic at AUG utilises the effect that a laser beam experiences a phase shift (ϕ) when passing through a plasma with a local electron density ($n_e(x)$).[62] The phase shift is quantified by:

$$\phi = \lambda_0 r_e \int n_e(x) dx \tag{3.2}$$

with λ_0 being the vacuum wave length, r_e the electron radius and x the spatial coordinate. This shift is measured through a Mach–Zehnder-type interferometer. The applied deuterium cyanide laser has a wavelength of $195\,\mu m$, for which a phase shift of 2π (between the light passing through the plasma and vacuum) corresponds to a line-integrated density of 5.72×10^{18} electrons/m^{-2}. The laser is split into six components of which five enter the plasma at different locations.

A possible source of errors for this diagnostic is the fact that only the modulo of the phase shift is measurable. This can lead to so-called "fringe jumps" (counting error by a multiple of 2π), which cause an incorrect reading. One measure to ensure a correct reading is to check the phase at the end of every measurement to determine whether it has returned to 0.

3.3 Electron Cyclotron Emission - ECE

During the time electrons gyrate around the magnetic field lines, they emit a characteristic frequency f, which is proportional to the magnetic field intensity $\boldsymbol{B}$.

$$f = \frac{le\boldsymbol{B}}{2\pi m_e} = \frac{\omega}{2\pi} \tag{3.3}$$

l being the harmonic number, e the elementary charge, m_e the electron mass and ω the angular frequency. With the plasma behaving like a blackbody source, the spectral intensity of a frequency $I(f)$ is temperature-dependent. Therefore, by spectral analysis of the millimeter wave intensity profile, it is possible to determine T_e.[63] By applying Planck's law, $I(f)$ is given by

$$I(\omega) = \frac{\hbar\omega^3}{8\pi^3 c^3} \frac{1}{\exp(\hbar\omega/kT_e - 1)} \xrightarrow{\hbar\omega \ll k_B T_e} \frac{\omega^2}{8\pi^3 c^3} k_B T_e \tag{3.4}$$

with k_B being the Boltzmann constant and c the speed of light. In eq. (3.4) Rayleigh-Jeans approximation of thermal emission was considered since modern-day fusion plasmas are optically thick, which gives a linear relation between $I(f)$ and T_e. This law holds true except for the plasma edge where the plasma becomes less dense and therefore optically thin, and a forward model has to be applied to correct the electron cyclotron emission (ECE) measurements.[64]

Due to the magnetic field being proportional to the inverse of the plasma radius, it is possible to derive a radial electron temperature profile with a single ECE line of sight. At AUG the ECE diagnostic observes the second harmonic (l=2), as the plasma emits at this mode like a blackbody source. The diagnostic utilises a multichannel heterodyne receiver covering a bandwidth of 89-187 GHz.

3.4 Poloidal Scrape-Off Layer Current

As in section 2.3.4 mentioned, there are poloidal currents in the SOL originating from various effects. At AUG these are measured through shunts that are attached to the target modules. Measurements are taken at four different toroidal positions and for the inner and outer divertor. These are then multiplied by the total number of modules. The signal is called I_{polsoli} (inner) or I_{polsola} (outer) at AUG. Although it has a low spatial resolution, its signal-to-noise ratio makes it a primary indicator to assess ELM frequency and intensity and it serves as a proxy for the target tiles' temperature in between ELMs.

3.5 Lithium Beam Emission Spectroscopy - Li-BES

The lithium beam emission spectroscopy (Li-BES) utilised at AUG is used to measure electron density profiles and density perturbations. The physical principle of the diagnostic is based on the de-excitation from the Li_{2p} state to the Li_{2s} of lithium atoms that are introduced into the plasma via a beam. As the lithium atoms collide with the plasma, they are excited into higher energetic states and undergo the process of radiative de-excitation (in the case of $\text{Li}_{2p \to 2s}$ within 27.11 ns). The reason for the choice of this transition is due to the Li_{2p} being the most strongly populated one and its characteristic photon wavelength of 670.8 nm which is in the visible spectrum and easy to measure.[65] Consequently, through spatial measurements of the characteristic line intensity and the application of a beam attenuation model, the electron density can be estimated.

Li-BES is comprised of a lithium beam injector and a new optical head measuring the characteristic line intensity. The Li-BES head consists of 3 rows with 28 channels in the middle row and 16 per row above and below.[66] The beam injects neutral lithium atoms at energies of 35-60 keV from the low field side, generating a current of 1.5-3 mA. The installed chopping system deflects the beam away from the optical system or modulates the ion extraction, allowing for background subtraction. The measurements taken from the upper and lower row of the optical head can be used to estimate the poloidal velocity, whereas the ones of the middle row are mainly used for density (-perturbation) analysis. Besides the new optical head, there is an older one, situated at the top of the vessel, which has a lower photon yield, but a better radial resolution. Within the scope of this thesis, both optical heads were evaluated simultaneously.

The reconstruction of the electron density from the line emission measurements is based on a probabilistic data analysis approach (Bayesian probability theory). The method involves comparing forward-modelled line intensity emission profiles against the measured data with the aim of finding a fit that resembles the measured profile. The forward-modelled data is calculated via a collisional-radiative model (CRM). This CRM computes the occupation density of 10 energetic states of the Li-atoms (including the Li_{2p} state).[67] The occupation density of Li_{2p} is proportional to the measured emission profile by the lithium beam diagnostic and since the CRM is dependent on the density and less sensitive to the temperature, the measured emission profile's underlying density profile can be derived by finding a proper fit to it.[68, 69] Through taking the measured and modeled quantities' uncertainties within the comparison into account, consistent data analysis can be assured, the influence of noise can be quantified.[68] The model for describing the Li beam attenuation uses well tested atomic data of [70]. As a final remark, due to the beam attenuation by the plasma in the investigated high density scenarios, Li-BES measurements are limited from the SOL to just inside the separatrix.

3.6 Thomson Scattering - TS

The Thomson scattering (TS) diagnostic at AUG is designed to study electron density and temperature. It is based on the Thomson scattering effect, which describes the interaction between free-charged particles and photons. As these particles are accelerated by the electromagnetic (EM) field of the photon, they in turn emit an EM-wave at a different angle, therefore scattering the initial one. The TS cross-section is proportional to the inverse of the scattered particle's squared mass and hence electron-dominant in the plasma. Due to the electron's velocity, the scattered photon experiences a spectral shift which ultimately leads to an overall Doppler-broadening of the emitted spectrum and the number of scattering electrons determines the intensity of the radiation profile.

The diagnostic consists of one edge and one core TS measuring setup. The one measuring the edge utilises 6 high-power monochromatic lasers (neodymium-doped yttrium aluminium garnet at AUG) and the core utilises 4.[71] The laser pulse lasts 10 ns at a rate of 20 Hz and has an energy below 1 J. The lasers are not fired simultaneously to avoid mutual interference. The scattered spectrum is measured by 11 channels of the edge and 16 channels of the core TS and then analysed by individual polychromators with 4 spectral channels. The density is then estimated by the scatter profile intensity and the temperature by fitting a non-Gaussian pulse shape to the spectral profile.[72] Calibration is needed in order to ensure correct measurement. The radiation intensity and therefore electron density estimation requires an absolute calibration of the channels. A relative calibration between the signal ratios of the 4 spectral channels provides accurate electron temperature measurements.

3.7 Integrated Data Analysis - IDA/IDI

Through the collation of complementary measurements by the above-mentioned diagnostics, a plasma-parameter dataset with enhanced temporal and spatial resolution is created. Since these measurements are based on different physical principles, agreement between them increases the confidence in the measured profiles. This verification process is performed with the assistance of parametric fits, this involves mapping the individual or combined data onto a common coordinate system (ρ_{pol} see eq. (1.4), using a previously determined magnetic equilibrium), as it allows for a comparison and validation of the individual diagnostics. This opens up the possibility of excluding inconsistent data and the formation of a subset. However, this approach does not take into account error propagation and specific diagnostic issues. It creates a non-standardised analysis procedure as it is up to individual decisions by the analyst who might not have the most expertise or knowledge of the diagnostics' characteristics. As these profiles are regularly used as input for further calculations, it opens up the possibility for non-negligible estimation mistakes. Additional disadvantages are that iterative calculations do not apply to large data sets and that there is a loss of information.

Hence, a concept of combining the differently measured parameters in a standardised approach at AUG is the Integrated Data Analysis (IDA) based on Bayesian probability theory. [73] IDA is initiated with an already mapped complete set of physical parameters containing kinetic profiles (e.g. pressure) and magnetic equilibrium describing quantities (e.g. plasma pressure and current profile). These parameters are mapped on the individual diagnostics coordinate system and then used to forward model the measured data. Through a likelihood probability distribution, these modeled data points are then validated against the measured experimental raw data.

Other Integrated Data analysis methods of which data was used within this work includes the Integrated Data analysis for Ion profiles (IDI) and the Integrated Data analysis for Equilibrium reconstruction (IDE). IDI uses measurements of the CXRS diagnostic to model the ion temperature and toroidal velocity via Gaussian process regression. IDE solves the Grad-Shafranov equation and current diffusion equation based on the concept of CLISTE [74, 75] with data as input from sources like the magnetic probes for poloidal and radial magnetic field, flux loops, pressure constraints from IDA and IDI and several others. [76] The produced equilibrium is considered highly reliable and has a standard temporal resolution of 1 ms, which is sufficient for the presented analysis.

Throughout this chapter, diagnostics have been presented that were utilised to generate plasma parameter profiles using integrated data analysis and to study ELM behaviour. An overview table showing the relationship between the diagnostics and the parameters of interest.

	n_e	T_e	T_i	v_T
CXRS			✗	✗
DCN	✗			
ECE		✗		
Li-BES	✗			
TS	✗	✗		

Table 3.1: Overview of the utilised diagnostics and the plasma properties of interest.

Chapter 4

Database

The following part presents the database that was used throughout the plasma behaviour analysis.

The general course of a discharge within the database consists of inducing the XPR through specific N_2 seeding, after which its position is actively controlled and brought to the predetermined height above the X-point via nitrogen puffing from the valves positioned in the divertor region. This progression is exemplarily depicted in fig. 4.1 via the green (XPR height) and red line (N_2 gas puff). The plot also showcases the behaviour between nitrogen puffing and the XPR height. As the XPR height varies, the change in the plasma edge values is monitored for subsequent analysis. Throughout every chosen discharge the plasma current, toroidal field, deuterium gas puff and q_{95} were kept constant. The exception being shot #39004, where the deuterium gas puff was varied. However, the time range with varying D_2 gas puff was discarded within the database (see fig. 5.1).
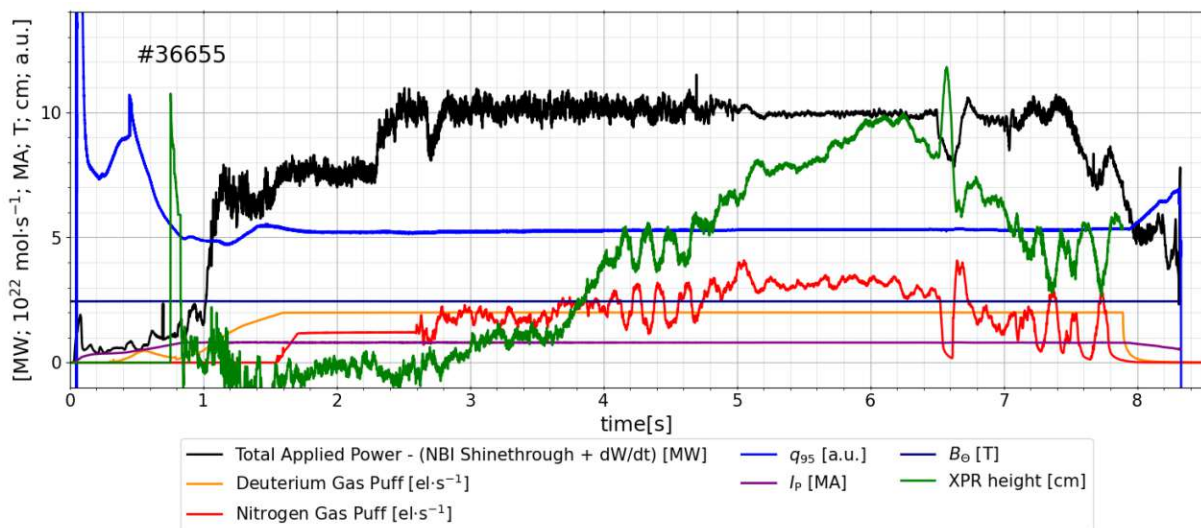
Figure 4.1: Exemplary discharge evolution of #36655.

Throughout the work of this thesis a total of 95 timewindows of 7 discharges were analysed. The selection of discharges was based on the fact that the largest number of discharges with an XPR existed for a plasma current of 800 kA and a B-field of -2.5 T. The discharges were heated through ohmic heating, electron cyclotron resonance heating (ECRH) and neutral-beam injection (NBI). Table 4.1 presents an overview of the discharge and plasma parame-

ters of the utilised discharges and table 4.2 shows the average value of heating, deuterium gas puff and safety factor over the 95 time windows. These time windows had an average length of 224 ± 46 ms and were chosen to have similar values in heating (except NBI heating), plasma current, toroidal magnetic field, deuterium gas puff and safety factor. The ECRH heating is similar over all time windows with 2.60 ± 0.26 MW. Only time windows of constant and consistent NBI heating of around 7.5 MW were selected and phases of NBI trips were discarded. However, the NBI heating in discharge #38116 & #38117 varied, due to their program being the investigation of high-power ELM suppression. In these two shots time windows of "increased" NBI heating power ($\sim$ 10 MW), in addition to the "regular" ($\sim$ 7.5 MW), were selected as well to expand the range of the database. The selected "increased" NBI heating time windows therefore have a total heating power (not accounting for shinethrough) of around 12.5 MW. The average applied heating power over all time windows is therefore 10.45 ± 1.04 MW.

The investigated time intervals had constant phases of deuterium gas puff of $2.08 \pm 0.08 \times 10^{22}$ el·s^{-1}. All discharges utilised nitrogen seeding to create the XPR, with two of them applying feed-forward seeding (#36166 and #38476) and the other five applying the XPR controller to actively control the position via feedback.

Shot #	P_{NBI} [MW]	P_{ECRH} [MW]	P_{TOT} [MW]	I_P [MA]	B_Θ [T]	Γ_{D_2} [$\times 10^{22}$ el·s^{-1}]	q_{95} [a.u.]
36166	7.45	2.65	10.07 ± 0.05	0.8	-2.4	2.06	-5.2
36655	7.45	2.38	9.81 ± 0.02	0.8	-2.4	2.00	-5.3
37441	7.40	3.07	10.47 ± 0.08	0.8	-2.5	1.94	-5.3
38116	7.45	2.62	9.94 ± 0.13	0.8	-2.5	2.14	-5.4
	9.90	2.62	12.49 ± 0.11	0.8	-2.5	2.14	-5.4
38117	7.30	2.87	10.17 ± 0.00	0.8	-2.5	2.14	-5.3
	9.80	2.87	12.65 ± 0.00	0.8	-2.5	2.14	-5.3
38476	7.30	2.26	9.52 ± 0.05	0.8	-2.5	2.15	-5.3
39004	7.40	2.82	10.22 ± 0.02	0.8	-2.5	2.14	-5.4

Table 4.1: Discharge and plasma parameters of the database. Discharge #38116 & #38117 are split into two rows due to different phases of NBI heating power.

The investigated plasmas were in H-mode and experienced small ELMs unless the XPR was raised to the ELM-free access condition height after which the ELM signature in the $I_{polsola}$ disappeared and detachment was achieved.
All shots are in H-mode and experience type-II ELMs unless the XPR was raised to the ELM-free access condition height after which the ELM signature in the $I_{polsola}$ disappeared and detachment was achieved.

Plasma Parameter	Value
P_{NBI} [MW]	7.85 ± 0.98
P_{ECRH} [MW]	2.60 ± 0.26
P_{TOT} [MW]	10.45 ± 1.04
I_P [MA]	0.799 ± 0.002
B_Θ [T]	-2.47 ± 0.02
Γ_{D_2} [$\times 10^{22}$ el·s^{-1}]	2.08 ± 0.08
q_{95} [a.u.]	-5.31 ± 0.06

Table 4.2: Average values over all timewindows for table 4.1

Chapter 5

Workflow and Methodological Approach

This section addresses the methodological approach in the plasma parameter and plasma stability analysis process. The first part describes the workflow in selecting and generating the time windows to assess the parameters for various XPR positions, choosing radial subregions of a near constant gradient to examine the spatial extent of the parameter variation and preparing the data for a standardized approach by normalizing it to allow for a more coherent comparison. The second part deals with the preparatory work for the MHD stability analysis through the codes HELENA and MISHKA.

5.1 Preceding Work of the Plasma Parameter Analysis

The grey boxes in fig. 5.1 indicate the chosen time intervals for the comparison.
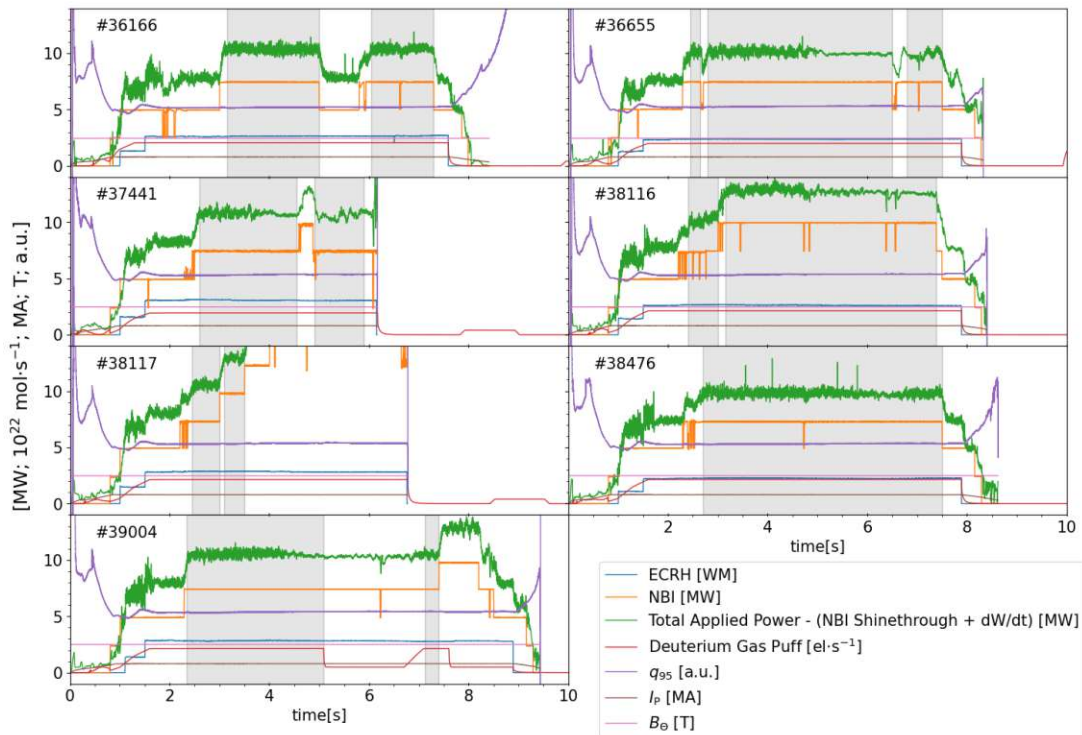
Figure 5.1: Compilation of all utilised discharges with time segments of interest (indicated by grey boxes).

The figure emphasises that major discharge parameters (heating, plasma current, toroidal

magnetic field, deuterium gas puff and safety factor) were similar throughout the comparison. These large time intervals were then subdivided into the previously mentioned 95 time windows of ~225 ms each having an at least 50 ms gap to its neighboring time window.

The plasma parameters which were analysed within the scope of this thesis are the electron density (n_e), temperature (T_e) and pressure (p_e), ion temperature (T_i) and toroidal velocity (v_T). The profiles of the electron quantities were taken from IDA and the ones of the toroidal velocity and ion temperature from IDI. The fitted profiles of the Integrated data analysis methods were then validated against measurements and found to be of good quality.

Following the validation, the profiles were binned into segments corresponding to the time intervals. The profiles within these roughly 255 ms time segments varied marginally over time, which resulted in the decision to create an average to represent the profile within the time window.

The next step consisted of determining the XPR position and its mapping to the normalised poloidal flux coordinate. This was achieved by locating the spatial maximum radiation peak through Gaussian fits of the AXUV measurements. The radial and vertical XPR coordinates were then mapped onto an equilibrium generated via IDE to get the ρ_{pol} coordinate. In each time window, the XPR position fluctuated marginally, which resulted in the approach of assigning each time window a well-defined XPR location.

The objective of this analysis was to assess the plasma parameters ($X, X \in \{n_e, T_e, T_i, p_e, v_T\}$) and their respective gradient (∇X) and gradient length ($\lambda_{\nabla X} = X/\nabla X$) in the region $\rho_{pol} \in [0.7; 1]$ in dependence of the XPR position. Therefore the range was split into 4 subregions (see fig. 5.2) to assess the spatial behaviour of the parameters. The width of each segment was determined so that the gradient is nearly constant over the selected area. The values in each subrange ($i, i \in \{A, .., D\}$) were then averaged ($\overline{X}_i$) in order to create data points representing the respective subregion. The radial segment's colour is consistent over the whole document.

Figure 5.2 displays the temporally averaged temperature profiles with the solid line representing the average and the shaded area around the profile the
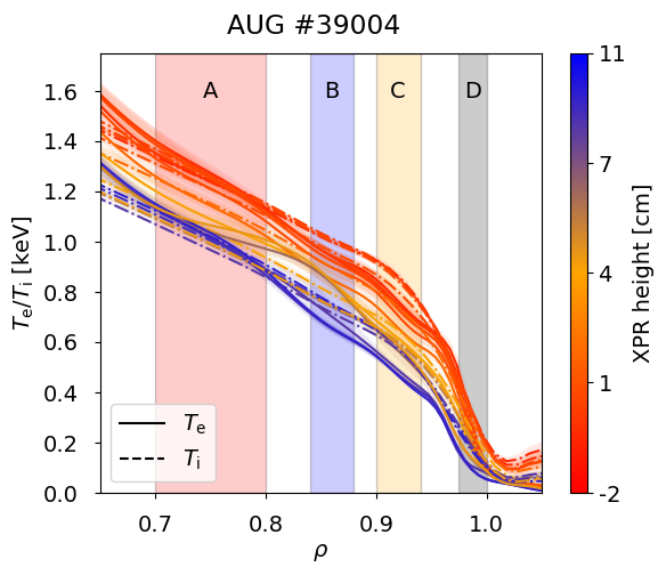

Figure 5.2: Example plot of the temporal binning and averaging process with indicated subranges of interest denoted with their respective alphabetical letter for the temperature profiles of #39004. The colour of the profile corresponds to the XPR height throughout the time window given by the colour bar.

local standard deviation. Due to the small standard deviation and hence fluctuation of the profile within the time window, the shaded area is almost not visible, therefore visually justifying the choice of taking the average within a time window. The colour of the profile indicates the position of the XPR throughout the time window (not to be mistaken with subregions' colour code). Additionally, the ranges of constant gradient (A-D) are presented (A: $0.7 \leq \rho_{pol} \leq 0.8$; B: $0.84 \leq \rho_{pol} \leq 0.84$, C: $0.9 \leq \rho_{pol} \leq 0.94$ & D: $0.975 \leq \rho_{pol} < 1.0$). In the following, the region A is also referred to as outer-core region and region D as pedestal region. The findings of this figure are discussed in chapter 6 as its purpose in this section is to solely

provide an example of the data analysis.

In order to display the different behaviour of a plasma parameter in between different subregions (and allow other comparisons regardless of the absolute value also), a normalisation process was introduced that enables a standardised approach as the values are shifted from the absolute scale to a relative one. The goal was to showcase the parameter evolution as the XPR moves above the X-point (XPR height ~0 cm) into the confined plasma.

The normalisation process is exemplarily illustrated in fig. 5.3 for the electron temperature in subregion C ($0.9 \leq \rho_{pol} \leq 0.94$). Each red and blue dot in subplot (a) of fig. 5.3 represents the spatially and temporal average of T_e in the selected subregion for a given time window for a certain XPR height. First, the time windows where the XPR is around the X-point were selected (marked as blue in subplot (a) of fig. 5.3) and then averaged (blue dashed horizontal line in subplot (a) of fig. 5.3). Then all values (red and blue data points) were divided by this average value, this shifts the y-axis from an absolute scale (see subplot (a) of fig. 5.3) to a relative one (see subplot (b) of fig. 5.3). The completed sequence is displayed in subplot (b) of fig. 5.3. The convention for this specific normalization process is indicated through $\| \|_{z_0}$.

This normalisation allows the identification and comparison of trends of a plasma parameter in terms of the XPR evolution in different subregions against one another or different plasma parameters. Prior to the normalisation, an in-depth analysis of the different subregion plasma parameter behaviour is not possible, as their absolute values are significantly different.
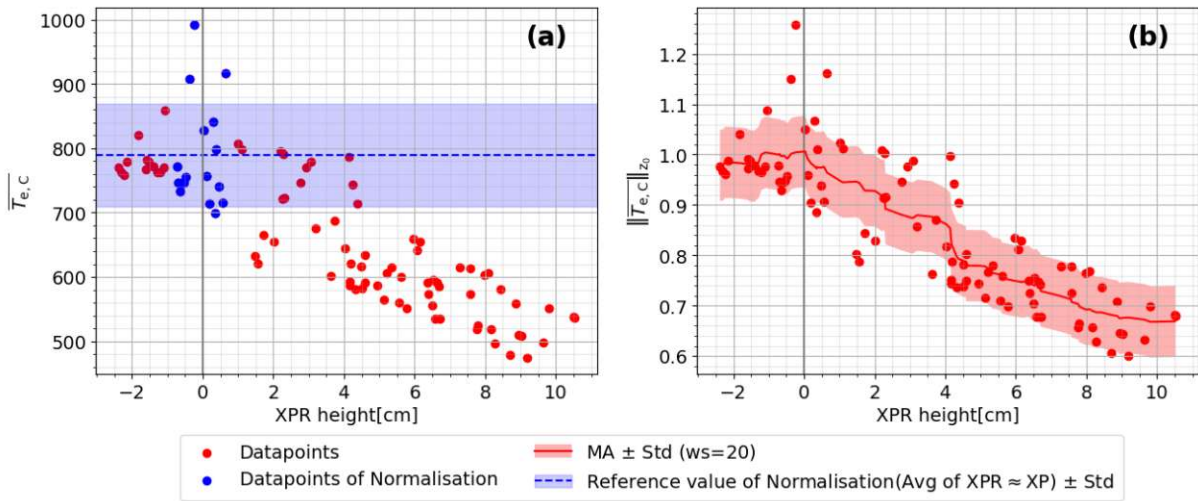

Figure 5.3: Normalization process to the average of the values of the time windows in which the XPR is in close proximity to the X-point (XPR≈XP). The average (Avg) and standard deviation (Std) of these values are indicated by the dashed line and the light blue shaded area. Figure (a) shows the absolute values and fig. (b) the normalised ones.

In chapter 6 the temporally and spatially averaged, and XPR height ≈ 0 cm normalised values have the following convention.

$$\left\| \overline{X_i} \right\|_{z_0} \tag{5.1}$$

To sum up, taking subplot (b) of fig. 5.3 as a reference, X being the plasma parameter (e.g. T_e), $\bar{\imath}$ the region of interest over which the plasma parameter was spatially averaged (e.g. C)

and $\|\,\|_{z_0}$ the normalization with respect to the values where the XPR is in close proximity to the X-point (XPR-z-height ≈ 0).

By taking the moving average of these values an XPR height trend can be visualised. This is displayed in fig. 5.3 (b) by the red solid line and the filled area around indicates the overall standard deviation.

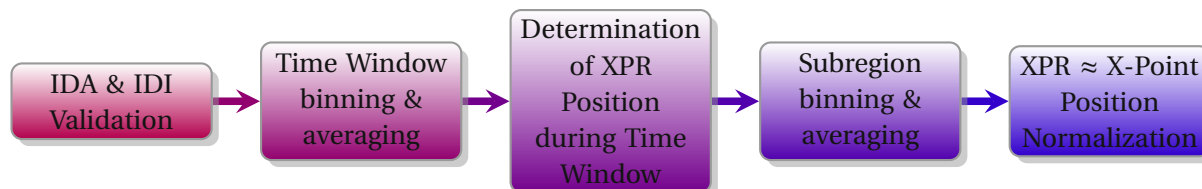The flow chart below (fig. 5.4) summarises the methodological approach to the plasma parameter analysis:

IDA & IDI Validation → Time Window binning & averaging → Determination of XPR Position during Time Window → Subregion binning & averaging → XPR ≈ X-Point Position Normalization

Figure 5.4: Flow chart of the data preparation approach.

5.2 Preceding Work of the Plasma Stability Analysis

Two computer programs were used to assess the MHD stability of the plasma at any given time point. The first one being the HELENA code [78, 79] which solves the normalized Grad-Shafranov equation with fixed boundary conditions. The necessary input for the code is firstly a predefined last closed flux surface inside the separatrix, which acts as the plasma boundary and secondly the pressure (more explicitly its gradient) and toroidal current ($\langle j_{tor} \rangle$) profile. IDA delivers a high-resolution pressure profile and the $\langle j_{tor} \rangle$ profile is provided via IDE calculations. HELENA then generates an equilibrium through iterative calculations of the Grad-Shafranov equation for several flux surfaces at a high resolution. In addi-

Figure 5.5: Exemplary graphic of the experimental and critical normalized pressure profiles (determined by HELENA). Adapted from [77].

tion to this refined equilibrium, HELENA also outputs the marginal ballooning stability for $n \to \infty$, which is then used to assess the local (for each flux surface) linear ideal ballooning stability via the Suydam method.[80] Within the scope of this work, the resulting information of this analysis was used to locate the operation point within s-α diagrams (as fig. 2.4) and compare the experimental pressure gradient profile (α_{exp}) against the critical normalized pressure gradient (α_{crit}) profile. α_{crit} denotes the upper boundary of α_{exp} above which the plasma becomes ballooning unstable. Figure 5.5 exemplarily shows radial profiles of α_{crit} and α_{exp}. It can be observed that the experimental α exceeds the critical value, indicating local ballooning instability.
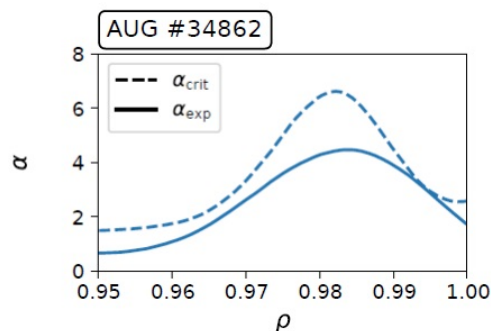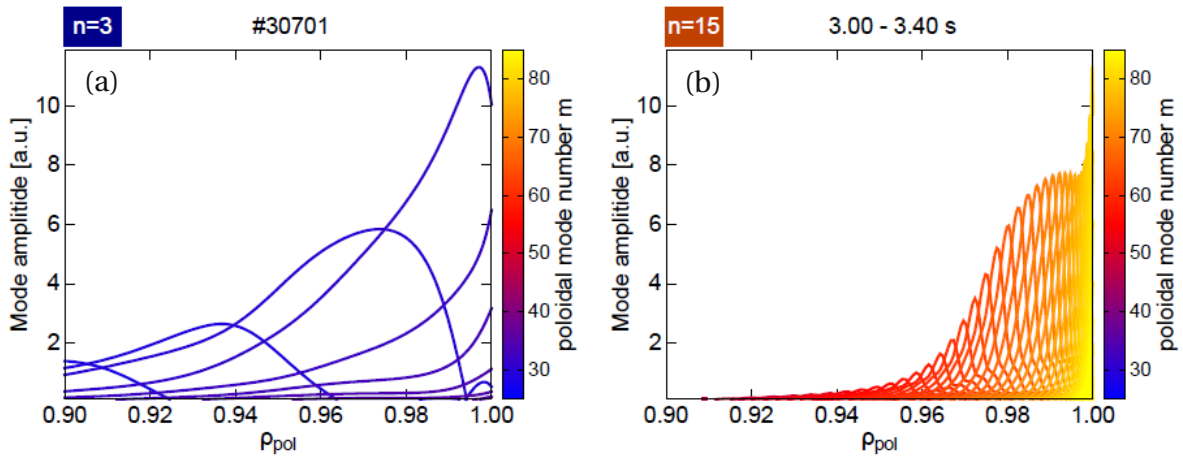
Figure 5.6: Display of the radial extent of different toroidal modes (n) depending on the poloidal mode number (m). (a) The peeling mode of $n = 3$ has only one dominant poloidal mode in the pedestal due to its broad radial extent. (b) The ballooning mode on the contrary is comprised of several poloidal modes due to their small radial width. Adapted from [81]

Further, the code MISHKA was applied, which analyses the global ideal MHD stability. In contrast to HELENA, which approaches the ideal MHD stability analysis from the perspective of infinitely small perturbations, MISHKA addresses the coupling of peeling and ballooning modes.[82, 83]. As the EPED model states (explained in section 2.1.1), the pedestal width plays a crucial factor in allowing the coupling of peeling and ballooning modes. Figure 5.6 illustrates the radial width of the peeling and ballooning modes. The peeling mode's prevalent mode extends over the whole pedestal width, whereas the ballooning mode consists of a superposition of multiple narrow modes.
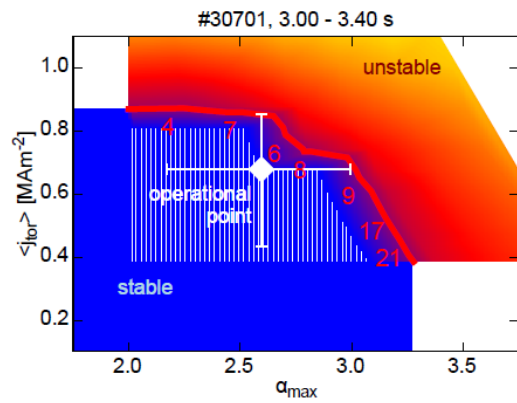
Figure 5.7: MISHKA generated j-α diagram for fig. 5.6. The stable region is separated from the unstable on via a red line (PB stability boundary). The numbers in red denote the most unstable mode for the equilibria corresponding to the j-α point. In this case, the operational point and its uncertainties (determined by the experimentally identified toroidal current and maximum pressure gradient) lie within the stable operational area. Adapted from [81].

MISHKA utilizes an iterative grid approach (j-α workflow [84]) as it calculates the linear growth rates of several toroidal modes ($n <$ 100) for a variety of equilibria in the $\langle j_{tor} \rangle$-α-domain.[83] The first step consists of altering the experimentally determined pressure and current density profile of the unaltered equilibrium (also called operational point within the context of MHD analysis) by a scaling factor and re-running them in HELENA to generate multiple equilibria. MISHKA then calculates the growth rate for multiple toroidal modes for the generated equilibria and determines the most unstable mode in each by selecting the one with the largest growth rate. The code then determines the stability of this equilibrium by the criteria of the Alfvén wave growth rate. If the growth rate of the most unstable mode exceeds around 5% of the Alfvén wave growth rate, the PB coupling destabilizes the pedestal and the corresponding equilibrium is said to be unstable. This generates a PB stability boundary just as in fig. 2.5. If the operational point of the unaltered equilibrium is within the PB boundary, it is said to be

PB stable (as illustrated in fig. 5.7).

The flow chart below (fig. 5.8) summarizes the methodological approach to the plasma MHD analysis:
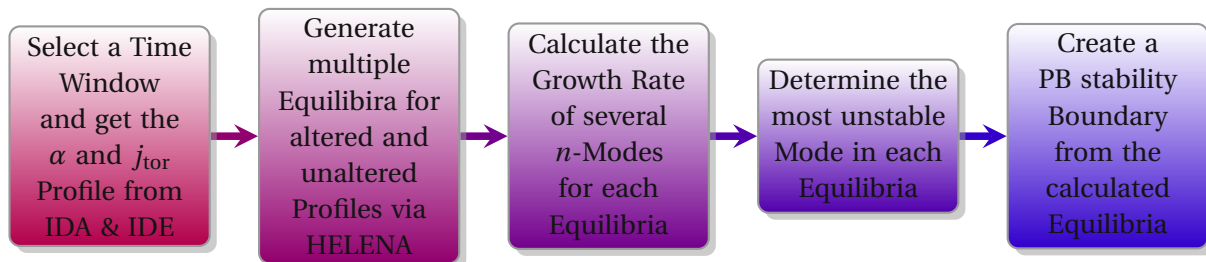

Figure 5.8: Flow chart of the MHD analysis preparation approach.

Chapter 6

Plasma Parameter and Stability Analysis

This chapter presents the results found throughout the plasma parameter and MHD stability analysis.

6.1 Results of the Plasma Parameter Analysis

The aim of the analysis was to investigate the evolution of the plasma parameters with changing height of the X-point radiator. Within the scope of this work the following plasma parameters ($X \in \{n_e, T_e, T_i, p_e, v_T\}$), their gradient ($\nabla X$) and gradient length ($\lambda_{\nabla X} = X/\nabla X$) were analysed. The gradient length indicates the radial extent of the decrease (assuming an exponential decay) after which the parameter would fall to a value of $1/e$, therefore demonstrating the pace and radial width by which the profile declines. In case of a declining gradient length, the profile decreases faster over the same radial width.

The XPR offers an operational regime with favourable properties such as increased line radiation (almost 100% of dissipated power fraction) and therefore decreased power flux into the divertor region (full detachment), real-time control of the XPR position, an ELM-free scenario and good impurity retention through improved neutral compression at marginally decreased W_{MHD} (reduction of ~ 10%), confinement ($H_{98} \approx 0.95$) and density (n_e reduction of ~ 15%).[23]

Figure 6.1 displays the previously mentioned influence of the XPR height on key factors of the plasma operation such as W_{MHD}, ELMs ($I_{polsola}$ as indicator) and the divertor temperature ($T_{Divertor}$). Some key events are:

- The divertor starts to detach at around 4 seconds as the XPR reaches a height of 4.5 cm above the X-point.

- The ELM-free scenario is reached as the XPR reaches a height of ~ 7 cm at around 5 seconds which is showcased by the $I_{polsola}$ signal losing the ELM signature.

- After dropping below an XPR height of 7 cm the ELM signature reappears in the $I_{polsola}$ signal and the target starts to partially attach.

These conditions were observed in every investigated discharge. The stored energy experiences a drop of 7-9% (in comparison to W_{MHD} at an XPR height of 0 cm) as the ELM-free regime is reached. The purpose of the total applied heating power (minus the NBI shinethrough and dW/dt) in the figure is to generally indicate that each discharge XPR analysis started with the reaching of 10 MW of heating and additionally clarify the dip of W_{MHD} and shift of the XPR at ~ 6.5 seconds due to an NBI trip.
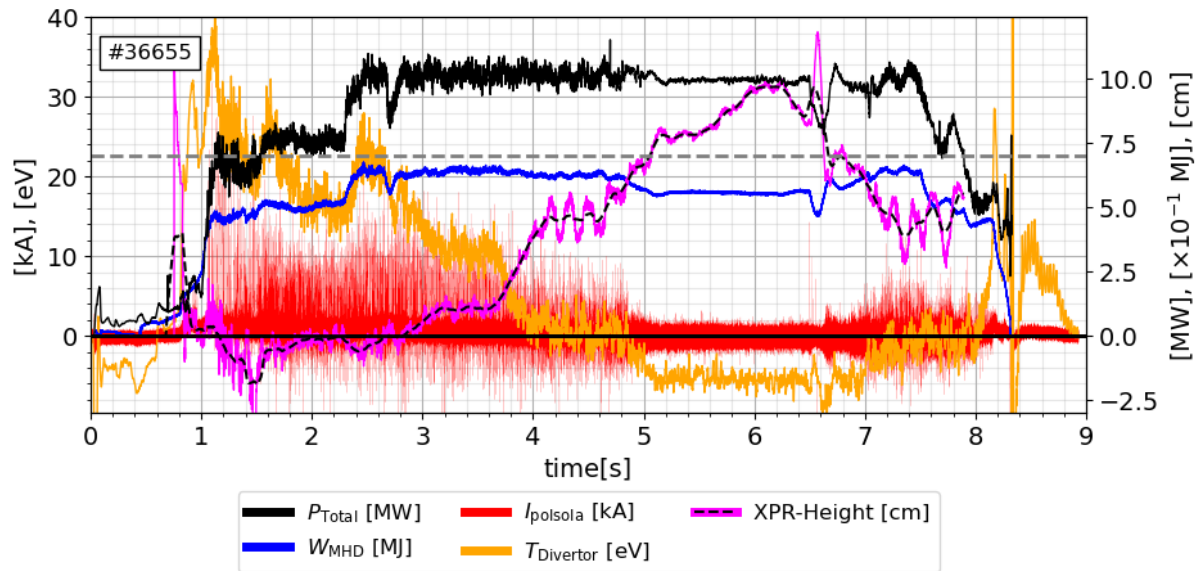
Page 40 of 66

Figure 6.1: Time evolution of discharge #36655's total heating power (P_{Total}), total stored energy by plasma from equilibrium (W_{MHD}), ELM indicator (I_{polsola}), divertor temperature (T_{Divertor}) and XPR height measurement (plus moving average indicated by black dashed line). The dashed grey horizontal line indicates the ELM-free access condition, which is an XPR height of around 7 cm. The units on the y-axes indicate which plotted line refers to which y-axis.

The following sections address the behaviour of the plasma parameter profiles and the behaviour of each plasma parameter in a specific subregion with respect to the XPR height above the X-point.

6.1.1 Parameter Profile Analysis with XPR-Evolution

In the following subsection, the behaviour of the overall plasma parameter profiles is treated, as the subregion analysis in section 6.1.2 allows for a more thorough breakdown. For this purpose, the discharge #36655 in fig. 6.2 is analysed as a representative example. The figure illustrates through colour-coding the behaviour of the profiles on the evolving XPR height. The colour-code convention of the subregions is consistent throughout the whole thesis and is of importance in the next subsection 6.1.2.

Electron and Ion Temperature

Looking at the electron and ion temperature it can be observed that the pedestal height decreases gradually. The profiles for an XPR height of around 4 cm show similar values in the outer-core region (denoted with the letter A) and therefore display a recovery despite the lower pedestal. However, the temperature profiles at an XPR height of 7-11 cm showcase a significant pedestal reduction. For these XPR positions the profile is not able to recover sufficiently, which reduces the profile's outer-core temperature by around 15-20%.

Electron Density

Regarding the electron density, as the nitrogen is puffed into the plasma it elevates the electron density due to the liberation of seven electrons as the nitrogen ion is fully ionised (in contrast to the introduction of a single electron in the case of hydrogen and its isotopes).

Initially, the pedestal height and width increase with an XPR height increase up to a value of 4 cm. This is followed by a decrease (for an XPR height above 7 cm) to approximately the values of an XPR height of 0 cm with the difference that the pedestal width is larger than for 0 cm. The profile elevation amounts to around 15% in subregion C and 20-25% in the outer-core region.

Electron Pressure

The electron pressure showcases a similar behaviour as the temperature profiles. The pedestal height descents gradually up to 4 cm, but is significantly lower for an XPR height above 7 cm. The steepness throughout the pedestal width decreases, but the profile shows a solid recovery as the gradient is sustained through subregion B and C, subsequently causing higher outer-core values. Above 7 cm the pressure profile and its gradient are lower through all subregions, displaying a substantial plasma pressure degradation.

Toroidal velocity

The response of the plasma in terms of the toroidal velocity shows an overall profile drop in speed in the subregions A and B and the significant pedestal degradation in subregion C. An inward shift of the local maximum and minimum (in-between subregion C and the separatrix) occurs with increasing XPR penetration. The local maximum previously centred at the separatrix moves inside with an XPR height above 7 cm.

The vertical red and blue lines indicate the maximum (ρ_{pol}=0.992) and minimum (ρ_{pol}=1) height of the XPR within the chosen time windows of discharge #36655. It can be observed that the inward shift of the local extrema of v_T is more pronounced than the one of the XPR. The XPR does only marginally move inside in terms of ρ_{pol} although it has a maximum height of 10 cm within #36655. The reason for the small $\Delta\rho_{pol}$ of 0.006 is the high flux expansion in the X-point vicinity.
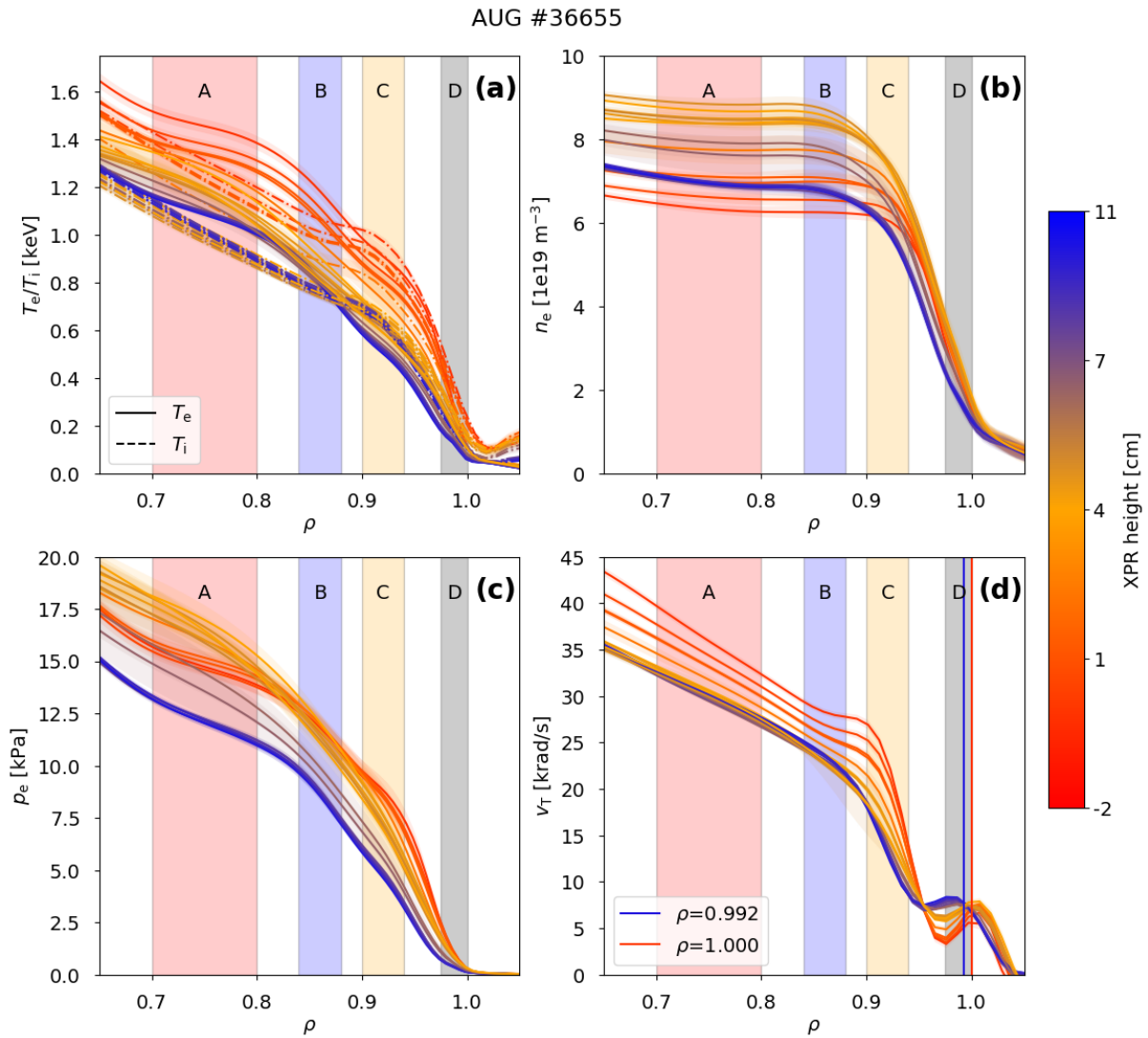
Figure 6.2: XPR evolution of the (a) T_e & T_i, (b) n_e, (c) p_e and v_T plasma profile for discharge #36655. The colour of the line corresponds to the XPR height in the respective time window according to the colour bar. The vertical lines in subplot (d) indicate the maximal and minimal XPR height mapped onto ρ_{pol}.

6.1.2 Plasma Parameter Subregion Behaviour with XPR-Evolution

This subsection addresses the behaviour of a plasma parameter in each subregion with XPR height.

Electron Temperature

The trend of the electron temperature, its gradient and gradient length is displayed in fig. 6.3. The absolute value of subregion D shows the steepest decline with XPR evolution. This is displayed in fig. 6.2 (a) as well, as the pedestal height decreases drastically with intruding XPR. The loss is linear with an absolute temperature drop of around 60% amounting to a decrease of 6% for every vertical cm of the XPR above the X-point. In contrast, the other regions show a much more gradual decline (up to an XPR height of 7 cm), with the outer-core (subregion A) having the lowest one. After reaching 7 cm in XPR height, subregion C proceeds with the decline, subregion B stays unchanged and the outer-core region seems to gain in temperature again. Another phenomenon that appears is a sudden and almost step-like drop in each subregion for an XPR height of around 4 cm.
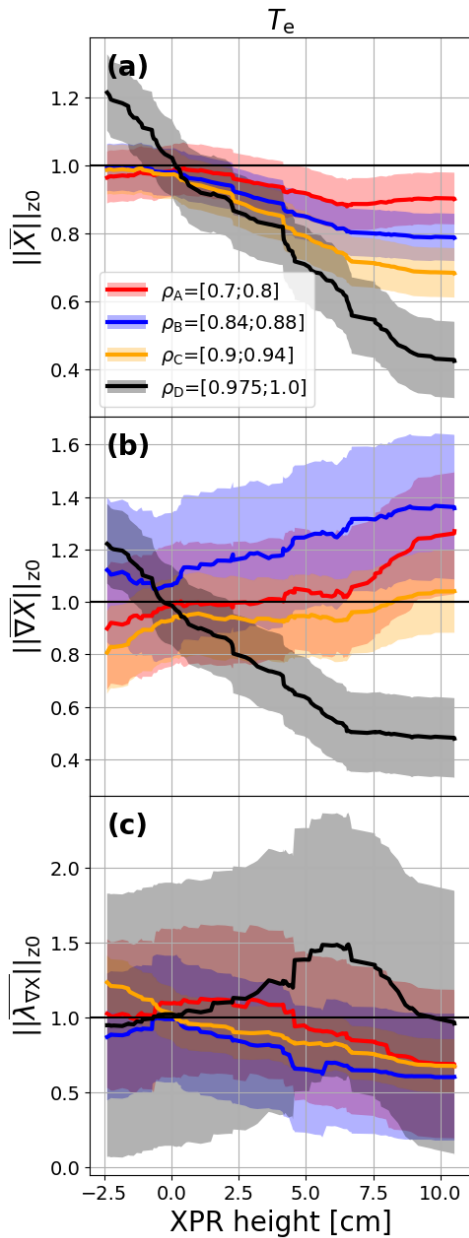
Analysing the gradient behaviour (see fig. 6.3 (b)), it can be observed that the gradient in the pedestal region (subregion D) has the biggest decline. This corresponds to the pedestal degradation which is visible in fig. 6.2. Moving further inside, the subregion C electron temperature gradient shows marginal response to the XPR position which could also be an artefact of the limited amount of data as its standard deviation of 15% covers the course of the gradient evolution. In contrast, subregion B shows a constant ascent with XPR height, amounting to an increase of 40% at 11 cm of XPR height. Subregion B's behaviour allows unaltered outer-core conditions due to a steep profile recovery despite the present pedestal degradation. The subregion A experiences almost no change in gradient until an XPR height of about 7-8 cm where a steep increase occurs.

The gradient length observations of fig. 6.3 (c) have significant standard deviations and carry therefore some uncertainty. The $\lambda_{\Delta X}$ evolution in subregion D has a standard deviation of roughly one, which prevents an accurate in-depth analysis of its XPR height evolution. However, for the moving average profile of the data of subregions D, it can be stated that it slowly increases by 50% which is followed by a sudden decline at an XPR height of ~7 cm. This could indicate that the radial extent of the profile steepness widens initially and then shrinks sig-

Figure 6.3: XPR height Analysis of T_{e}. Plot (a) displays the course of the average temperature in a subregion, (b) the gradient and (c) the gradient length.

nificantly. Subregion A-C's gradient length showcases a gradual descent of about 25%. The dip in subregion B's gradient length course can be attributed to the high fluctuation in the data. Each gradient length course indicates that less radial width for the profile recovery is needed and hence they recover faster with progressing XPR penetration. As a final matter, subregion A's gradient length declines with the exemption in the range up to an XPR height of 0-4 cm where it is elevated by ≈10%, however, its course lies within the standard deviation and carries therefore significant uncertainty.

To summarise, the plasma reacts to an increasing XPR penetration with a linear descent in the electron temperature. The pedestal region experiences the highest degradation since the XPR acts as a heat sink in its vicinity. The reason for this is the increasing energy loss through line radiation. The dip at an XPR height for subregions A-C and the step-like descent for subregion D that occurs at 4 cm, coincides with the divertor detachment allowing for an assumption of a change in the heat removal mechanism. However, the outer-core region seems to be unfazed by the XPR penetration as its average value only drops by around 10% until an XPR height of around 7 cm after which it seemingly increases again. These conditions can be maintained through the development of steeper gradients, which can be seen in the gradient and gradient length subplot which showcases increasing values with XPR height in subregions A-C. This offers the chance of an XPR-height-independent temperature in the core.

Ion Temperature

The ion temperature displays a similar behaviour to the XPR penetration as T_e with the exception of the temperature loss being less profound and that the outer-core and subregion B seem to even increase after an XPR height of 7 cm.

The course of the gradient in subregion D looks familiar to the one of T_e. For subregions B and C, their ion temperature gradient stays unchanged until the XPR is at a height of 7 cm after which an abrupt ascent of around 30-40% occurs. Subregion C shows an improved gradient increase compared to its T_e counterpart, whereas subregion A's gradient does not increase as much as it does in fig. 6.3 (b). The reason for this is the improved profile recovery of subregion C, which in turn improves the outer boundary conditions in subregion B, whose steep gradient provides an already improved condition for the outer boundary of subregion A so that it has to rise less steeply since the conditions are already very profound.
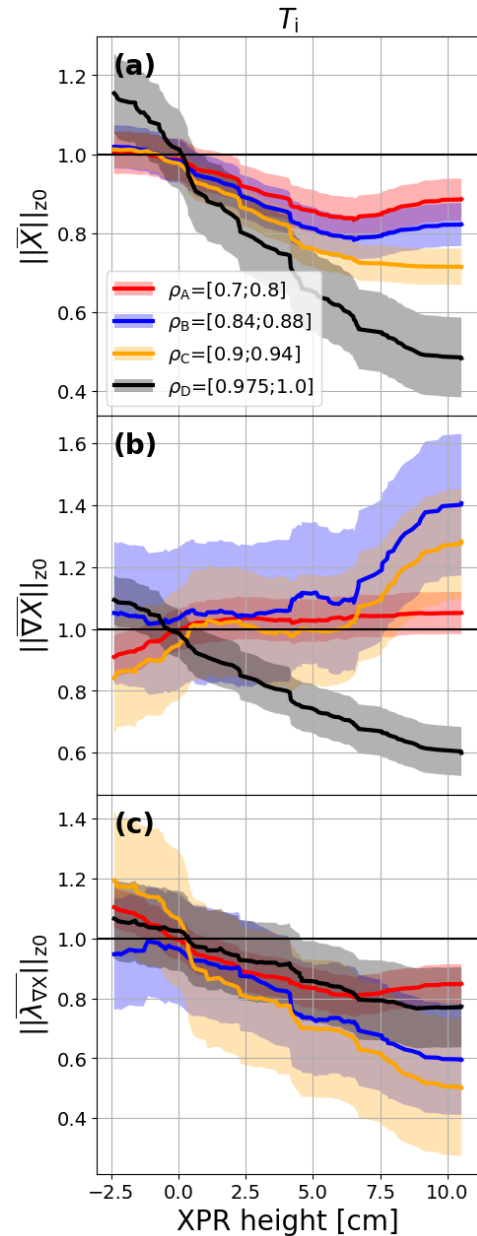

Figure 6.4: XPR height Analysis of T_i. Plot (a) displays the course of the average temperature in a subregion, (b) the gradient and (c) the gradient length.

The gradient length plot for the ion temperature allows for a more in-depth analysis as its standard deviation is significantly lower than that of the electron temperature. Every subregion showcases that the gradient length shrinks with XPR penetration, resulting in the conclusion that the radial width (which the ion temperature needs to recover) shrinks.
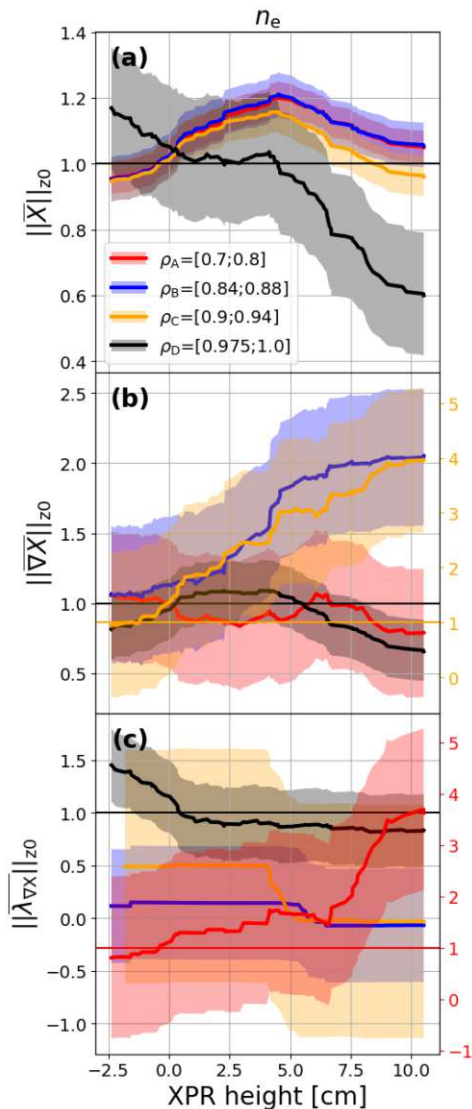
It can be concluded that both ion and electron temperature display a similar course, except for a stronger increase of T_i after an XPR height of 7 cm. The gradient profiles deliver an explanation for this phenomenon as the temperature recovery already occurs in subregion C (due to an increase of the gradient), which improves the conditions in subregion B which are passed on to the outer-core.

Electron Density

Regarding the electron density, a clear trend of the inner subregions A-C appears. The density in each subregion rises by about 20% until an XPR height of 4 cm is reached, after which it returns to values for an XPR height of 0 cm. This trend can be observed in fig. 6.2 (b) as well. Within the pedestal region, the situation looks differently as the pedestal value initially stays unfazed perhaps even increases slightly (uncertainty due to high standard deviation) and abruptly declines with an XPR height of 4cm. This descent ends with a density loss of around 40%. The reason for this course is the cooling of this area to levels allowing for recombination due to the XPR.

The gradient evolution of the outer-core region has a high uncertainty therefore preventing clear statements of the profile course. However, the electron density has a very flat profile within this range which seems to be unchanged over the whole XPR penetration scale. In contrast, subregions B and C showcase a steep increase, doubling and even quadrupling their initial gradient. The increase in subregion C addresses the pedestal and hence encompasses the steepest gradients, which is why its course is plotted against the second y-axis. The huge gradient of subregion C is the reason for the initial ascent of n_e in subregions A-C for an XPR height of 4cm and the just gradual decrease of subregions A-C's density values despite the steep decline of the pedestal values. The reason for this gradient development in subregion C is the presence of an ionization front. The gradient of the pedestal region displays an initial ascent up to 4 cm followed by a descent which originates from the enlargement of the recombination area and shift of the ionization front.

Gradient length analysis is subject to large uncertainty in subregions A-C and would therefore allow only vague assumptions. The coloured y-axis on the right of fig. 6.5 in subplot (b) and (c) of fig. 6.5 corresponds to the equally coloured line. This approach was chosen

Figure 6.5: XPR height Analysis of n_e. Plot (a) displays the course of the average temperature in a subregion, (b) the gradient and (c) the gradient length.

as it would have distorted the overall y-axis and hence made the visual analysis impracticable. The reason for this is the relatively low gradient in these areas which generates a high fluctuation in the calculation process. The exception is the pedestal gradient length, which decreases by an amount of 15% after the initial XPR penetration and remains at the level, meaning that the profile increases at the same rate over a shorter radial width with increasing XPR height.

Summarizing the findings and their triggering mechanism, the reason for the density elevation in subregions A-C for up to an XPR height of 4 cm stems from the location shift of the ionization front into the confined plasma (see figs. 2.17 and 2.18) therefore supplying large amounts of electrons. Due to the fact that the effective charge increases with XPR height, as neutral nitrogen atoms (carrying seven times more electrons than hydrogen) are able to enter the confined plasma, this effect intensifies. The pedestal area shows an immediate response with XPR penetration. An explanation for the decrease in density in subregion D (see in fig. 6.5 (a)) could be the increase in recombination and/or a change in the recycling pattern in the divertor. To investigate this in detail, 2D modelling is necessary.

Electron Pressure

The electron pressure combines the effects of the electron density and temperature. It can be observed that the subregion D pressure degrades severely amounting to a loss of 7.5% per cm of XPR height. The subregions A-C showcase an increase up to an XPR height of 4 cm, which is followed by a gradual decrease. The outer-core region experiences the biggest increase of 10% and returns to a relative value of one at around 7 cm which coincides with the ELM-free access condition.

The gradient in the pedestal decreases at a similar rate as the pressure, originating from the pedestal degradation (see fig. 6.2). Moving inwards, subregion C's gradient showcases an increase of ~25 % which plateaus at values of 5 cm of XPR height. The steepest profile recovery occurs in subregion B as its gradient ascents by a factor of 50% with an XPR height of 5 cm which then plateaus as well. With the outer-core re-

Figure 6.6: XPR height Analysis of p_e. Plot (a) displays the course of the average temperature in a subregion, (b) the gradient and (c) the gradient length.

gion being elevated through subregion B's boundary condition, its gradient only elevates slightly by around 20%. These trends are also clearly observable in fig. 6.2. In this graphic the pedestal degrades but outer-core values are maintained

Regarding the gradient length, all inner subregions A-C display a downward trend, meaning that the profile needs a smaller radial width to recover with increasing XPR penetration.
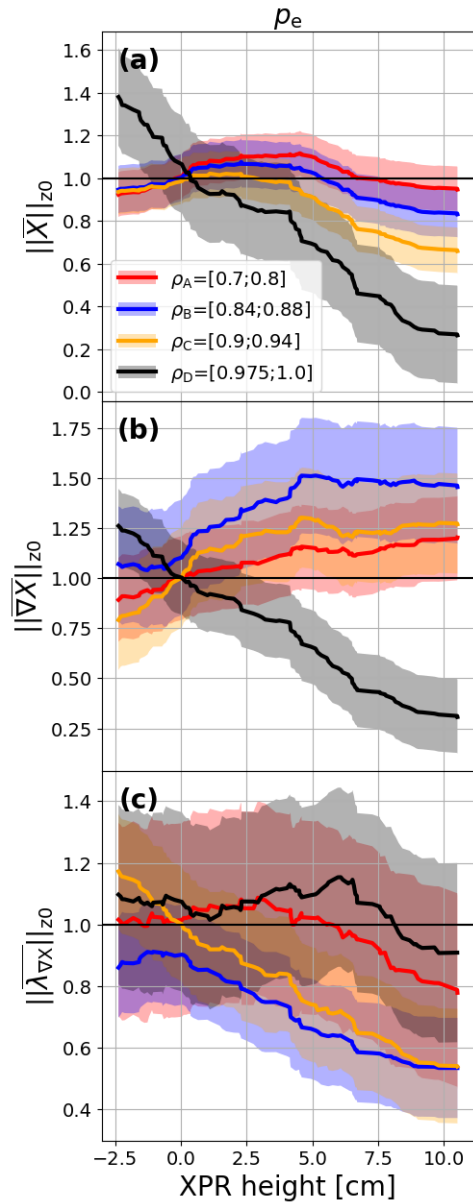
Only the pedestal region displays an ascent of 10% (used with caution due to high uncertainty), meaning the pressure in the pedestal area needs a larger radial extent to recover. This course continues up to the ELM-free access condition of an XPR height of 7 cm, after which it drops by 20%.

The findings of the plasma pressure with the outer-core increase and pedestal degradation open up the possibility of future operation of an unperturbed core plasma without ELMs and with a detached divertor.

Toroidal Velocity
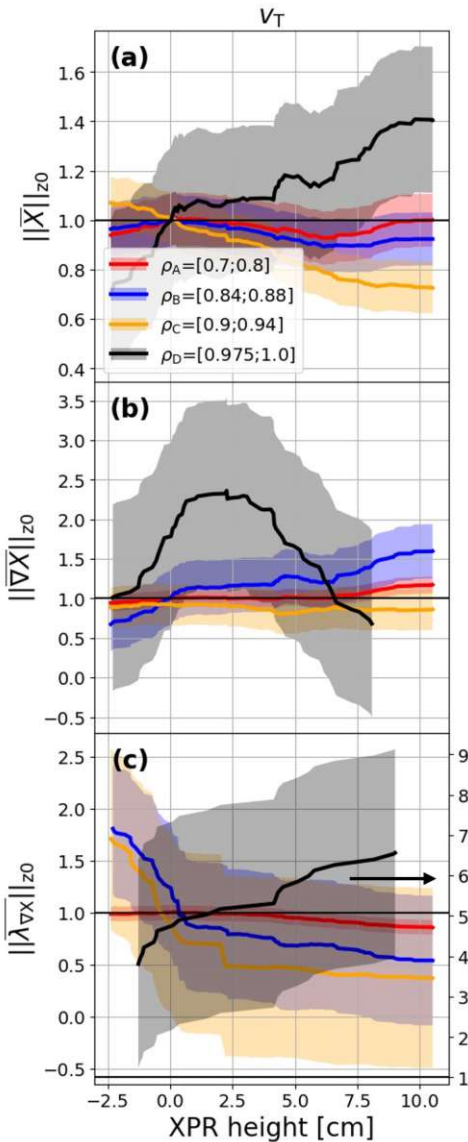
Figure 6.7: XPR height Analysis of v_T. Plot (a) displays the course of the average temperature in a subregion, (b) the gradient and (c) the gradient length.

The toroidal velocity in subregions A-C decreases with increasing XPR height, with the increasing descent moving from the inside out. The outer core region reaches its initial XPR penetration values with an XPR height of ~8 cm, whereas the subregion C drop amounts to almost 30%. Subregion B's decrease settles at around 10%. However, the velocity in the pedestal region increases in an almost linear trend by 40%. The reason for this is the shift of the local maximum of v_T towards the inside.

For subregion A the gradient of v_T seems to be unfazed by the XPR penetration. Subregion B's gradient course showcases an increase of around 50%. Both progressions can be observed in fig. 6.2 as well. The gradient in subregion C descents by a value of 10-20%, which corresponds to the pedestal degradation. As the local maximum in the pedestal region of v_T shifts further inward, the gradient changes accordingly. This amounts to an initial increase of 100% up till an XPR height of 2.5 cm after which the gradient descends to its initial value at an XPR height of around 6 cm.

Regarding the gradient lengths, it can be observed that subregion D has a significant uncertainty. Here, the approach for plotting a subregion against the right y-axis was chosen again, due to subregion D's high values. However, its trend points towards an almost sevenfold increase by an XPR height of 9 cm. The gradient length in subregion B descends gradually at a rate of 6% per cm, whereas the course in subregion C showcases a step-like decrease at 2 cm which is followed by a plateau. The outer-core gradient length stays unfazed by the XPR penetration.

In conclusion, the v_T pedestal (located in subregion C) degrades severely by almost 40% which is also showcased in the pedestal gradient. The inner subregions experience this in the form of lower boundary conditions. Looking at the pedestal region a shift of its local maximum can be observed, which is also reflected in the data. A possible explanation for this could be

a change in the plasma flows in the pedestal region. To determine whether the Er profile changes, also measurements of the poloidal velocity would be necessary, which is out of the scope of this work.

The overall conclusion states, that the electron and ion temperature decrease with XPR height and that the density increases initially up to an XPR height of 4 cm after which it descents to the reference values. There is an increase of electron pressure up to an XPR height of around 4 cm which coincides with the divertor detachment, after which a gradual loss of these improvements occurs. The pedestal region showcases clear and constant degradation with XPR penetration. However, over the course of the inner subregions B & C, the profile is able to recover, allowing for an unfazed outer-core region up to an XPR height of 7 cm (after which a marginal degradation occurs) which subsequently suspends the feeding of MHD instabilities as the value of α (normalised pressure gradient) decreases sufficiently (see section 6.2 for in-depth analysis). The profile recovery expresses itself by the prevailing gradient and gradient lengths in subregion B & C, as these cause the pressure to rise faster and steeper, while requiring a smaller radial distance. The pedestal degradation ultimately also affects the plasma flow velocities, which is visible through the shift of the toroidal velocity maximum in the pedestal region.

6.2   Results of the Plasma Stability Analysis

Throughout the following section, the findings of the MHD analyses are presented. These include ballooning stability analysis of HELENA and PB analysis of MISHKA. In total 10 different time windows (four in #36655, three in #38116 and #39004) were analysed within the scope of this work. The MHD stability behaviour is representatively showcased on four time windows (TW) of discharge #36655. These are displayed in fig. 6.8). The XPR height in each time window corresponds to the following values:

TW[#]	Time window [s]	XPR height [cm]	XPR position [ρ_{pol}]
1	3.15-3.45	0.31	1.000
2	4.10-4.40	3.21	0.999
3	5.10-5.50	8.06	0.994
4	5.95-6.25	10.14	0.992

Table 6.1: Database of the exemplary MHD stability analysis.
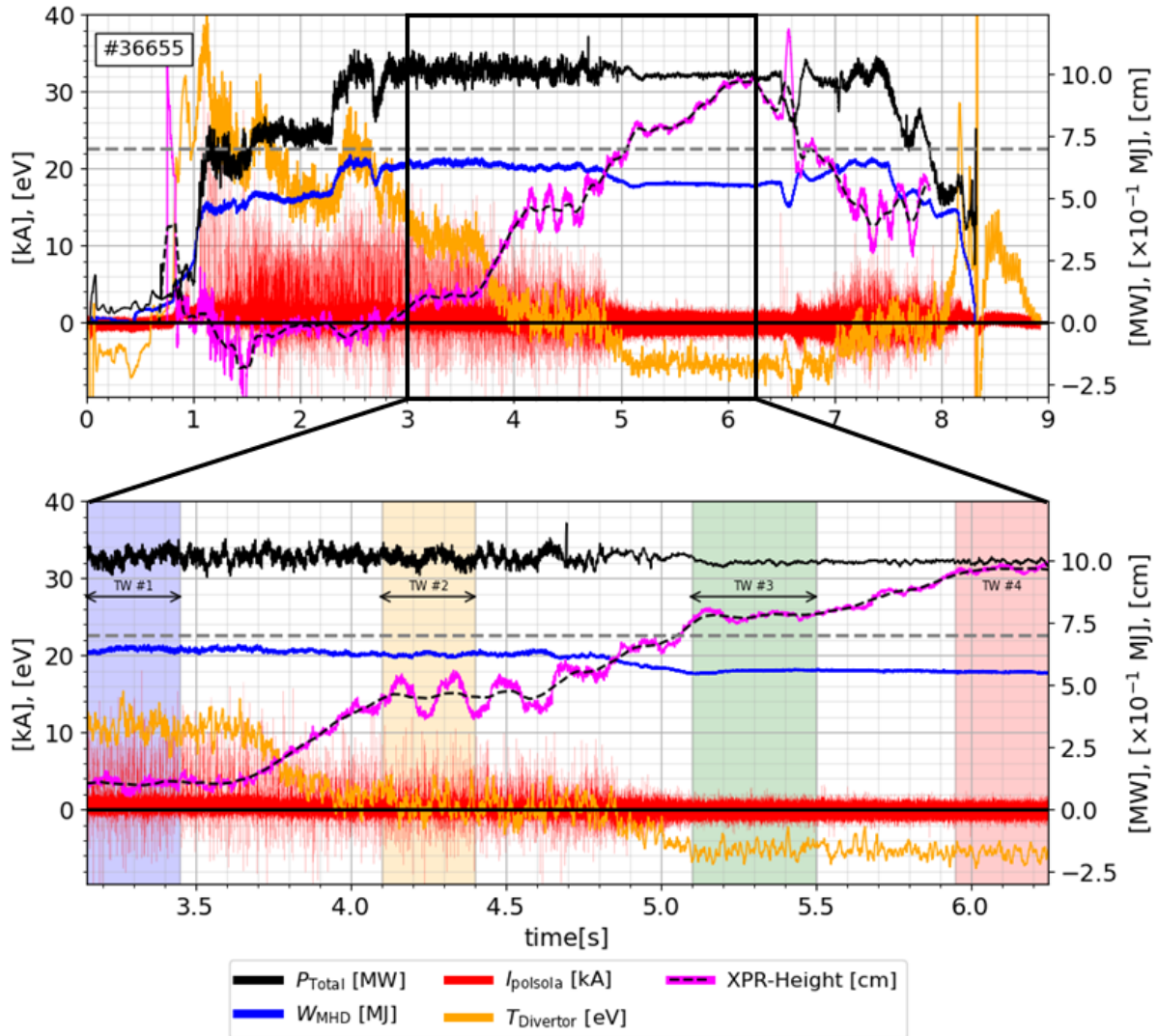
Figure 6.8: Time evolution of discharge #36655 of several parameters similar to fig. 6.1. The time range (3.0-7.0 s) is highlighted within which four time windows for the MHD stability analysis were selected. These time windows (TW #1-#4) were chosen to represent different stages of the XPR penetration.

6.2.1 Ballooning Stability Analysis with XPR-evolution

Analysing the Operational point with XPR-evolution

A measure of quantifying the ballooning stability for specific conditions is to determine the operational point within an s-α diagram. Figure 6.9 showcases the operational point at the location $\rho_{pol} = 0.975$ for four different time points all with different XPR heights. The heatmap colour is determined by the marginal ballooning stability factor F_{marg} which indicates the ballooning stability of a certain location within the s-α plot. F_{marg} is defined as the ratio between the critical and experimental normalised pressure gradient ($F_{marg} = \alpha_{crit}/\alpha_{exp}$). A value of above one indicates that the plasma is ballooning stable, whereas a value of below one ballooning instability indicates. $F_{marg} = 1$ presents the marginal limit of ballooning stability.

The first subplot of fig. 6.9 showcases the plasma's operational point for an XPR within the vicinity of the X-point. It is in a state of ballooning instability, which can be seen by the operational point being positioned closely to the marginal ballooning stability limit and the ELM signature within the $I_{polsola}$ signal (see fig. 6.8). The uncertainty of this operational point also offers the possibility that it even lies within the region of instability.

For the next time window, the XPR is positioned ~3 cm above the X-point corresponding to an ρ_{pol} position of 0.999. The divertor temperature in fig. 6.8 indicates that the divertor is in partial or full detachment and the ELM signature intensity within the $I_{polsola}$ signal has decreased slightly. The operation point has shifted marginally away from the stability boundary, but still appears to be in its vicinity stating that the plasma is still ballooning unstable.

For time window #3 the plasma has reached a state of ballooning stability as the ELM signature in fig. 6.8 has vanished and the operational point plus its corresponding uncertainty are located significantly away from the ballooning stability boundary. The XPR height corresponds to around 8 cm which is above the ELM-free access condition.
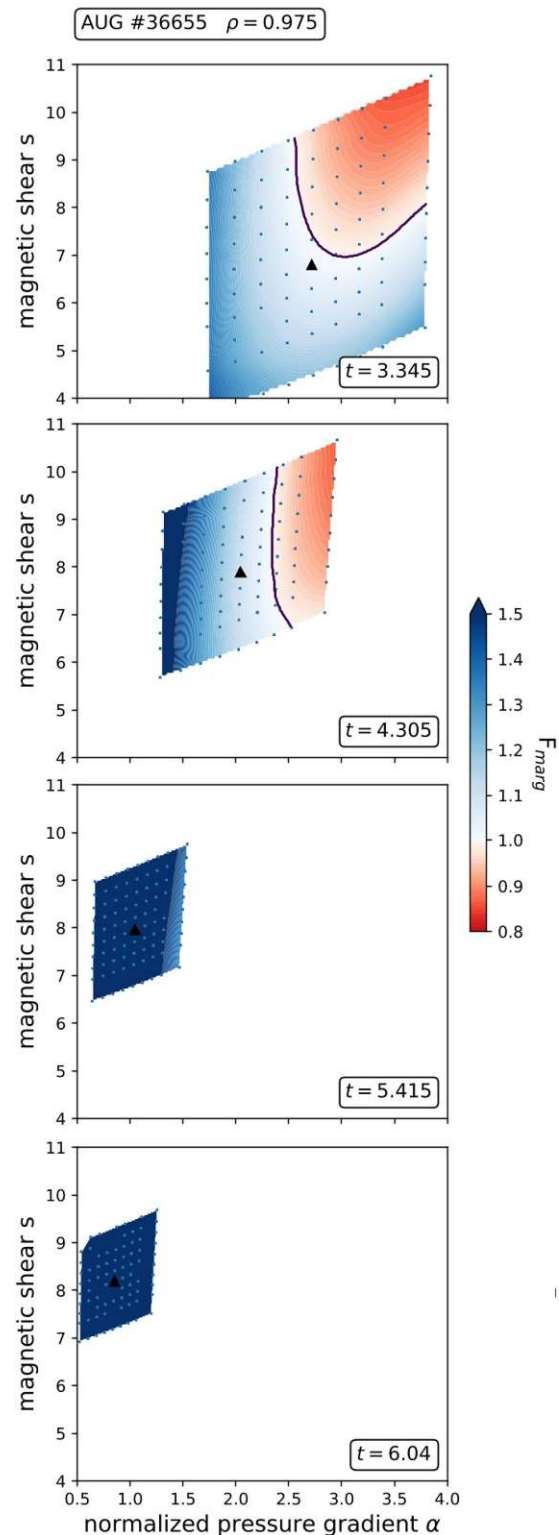

Figure 6.9: s-α diagram for discharge #3665 for four different time windows. The solid line indicates the marginal ballooning stability limit ($F_{marg} = 1$).

In the final subfigure of fig. 6.9 the operational point is even further distanced away from the ballooning stability boundary. The I_{polsola} and divertor temperature have changed marginally in comparison to time window #3, indicating no significant benefit for the divertor in terms of a higher X-Point height than 8 cm.

To conclude, the operational point shifts towards the first region of ballooning stability with increasing XPR height.

Operational point course with XPR-development in terms of shear and α
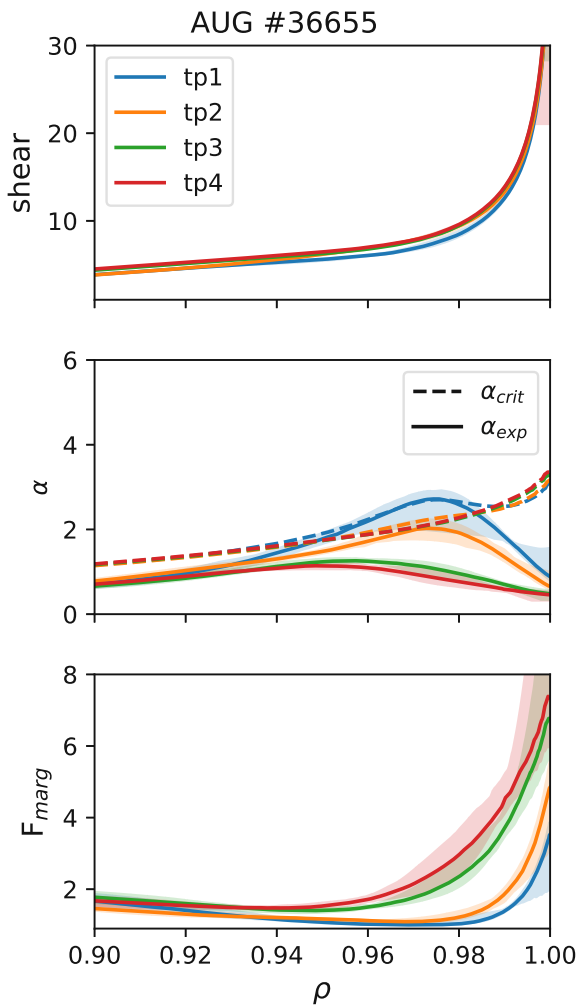
Figure 6.10: Shear, normalised pressure gradient and F_{marg} profiles of time points (tp) in the time windows of table 6.1. The colours of the profiles correspond to the time windows marked in fig. 6.8.

Figure 6.10 showcases the profiles of parameters of interest in the ballooning stability analysis. It can be observed that the shear only changes marginally over the course of the XPR penetration. In contrast to the profile of the normalised pressure gradient, which decreases significantly with the penetration of the XPR. For time point 1 the α_{exp} profile exceeds the critical value around $\rho_{\text{pol}} = 0.97$, which is the reason for the plasma's ballooning instability. Although the α-profile for point #2 is lower, its critical value boundary is also reduced which causes the plasma to exceed the stability limit as well. However, in the instance of TW #3 and #4, the profile of α_{crit} remains similar to TW #2's while the profile of the normalised pressure flattens, which subsequently causes the plasma to become ballooning stable. This can also be observed in the F_{marg} subfigure as the profiles of TW #1 and #2 reach values of $F_{\text{marg}} \sim 1$, whereas the ones of TW #3 and #4 remain at a considerable distance.

Figure 6.11 further displays the increase of the F_{marg} profile with XPR height. It can also be observed that the maximum of instability moves radially inward as the brightest spot in TW #1 in fig. 6.11 is situated in the range of $\rho_{\text{pol}} \in (0.96, 0.98)$ and for TW #3 and #4 in the perimeter of $\rho_{\text{pol}} \sim 0.95$ to $\rho_{\text{pol}} \sim 0.94$.
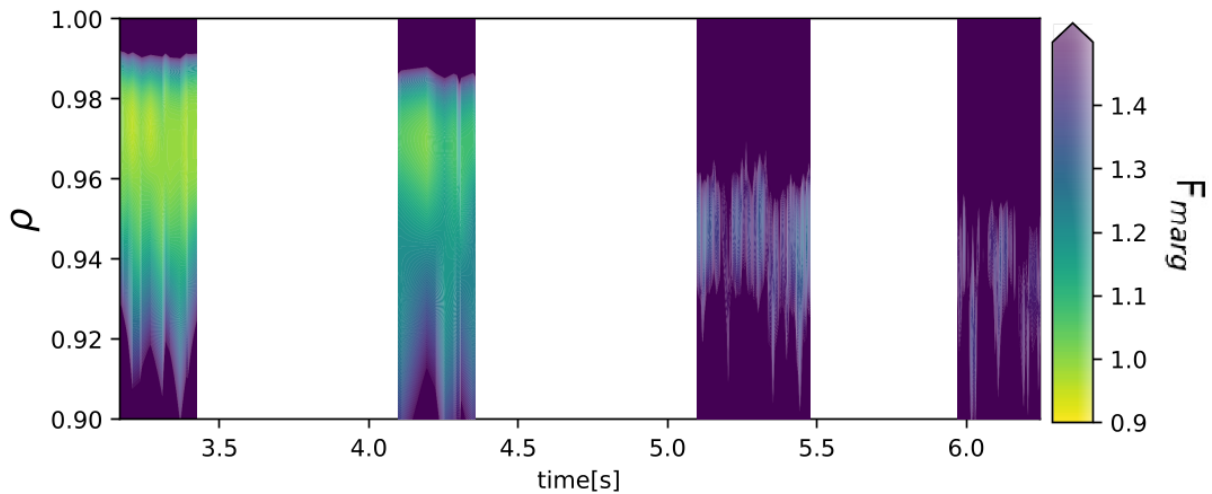
Figure 6.11: Temporal evolution of the marginal ballooning stability factor profiles throughout all time windows. The average time window value and its standard deviation are plotted in fig. 6.10.

6.2.2 Peeling-Ballooning Stability Analysis with XPR-evolution

In order to determine the PB stability of the time windows, the code MISHKA was utilised to calculate the operational point in the j-α space. Figures 6.12 and 6.13 showcase the MISHKA analysis for TW #1 and #4. It can be observed that initially the operational point is situated at the ballooning boundary as its toroidal mode with the highest growth rate (grrate) is of high value ($n = 20$) which is characteristic of ballooning modes. As the XPR is further introduced into the confined plasma, the operational point shifts as the plasma's pedestal pressure gradients decrease as well as its pedestal current. The plasma subsequently moves towards a PB stable operation as the growth rates of the analysed modes are significantly smaller than the ones of the Alfvén waves (see section 5.2 for the criteria of determining PB stability).
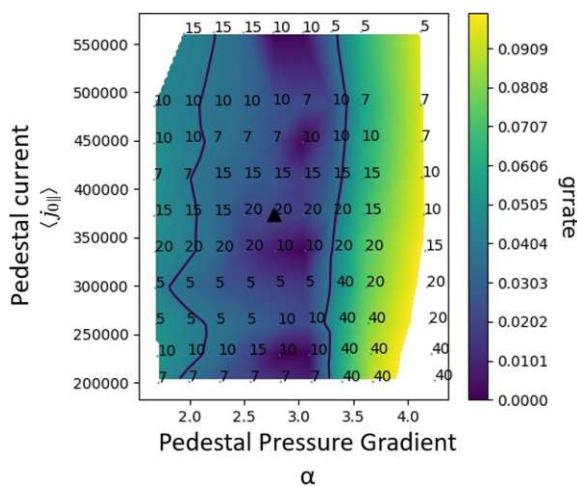
Figure 6.12: Operational point of TW #1 for discharge #36655 in MISHKA generated j-α diagram.
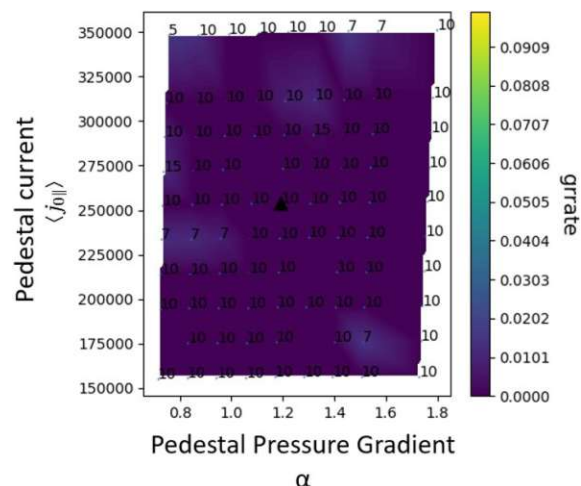
Figure 6.13: Operational point of TW #4 for discharge #36655 in MISHKA generated j-α diagram.

The MHD stability analysis concludes that with increasing XPR height, the plasma becomes increasingly ballooning and PB stable.

These findings in terms of the ballooning stability are support by the following points:

- Shift of the operational point in fig. 6.9 away from the marginal ballooning stability boundary,

- Undercutting of the α_{crit} profile by the corresponding α_{exp} profile, and

- Change of the F_{marg} profile in fig. 6.10

These findings are additionally confirmed by the conclusion of section 6.1.2 which showcases the pedestal pressure (and its gradient) decrease with evolving XPR penetration, hence ending the energy source for large MHD instabilities. In terms of the peeling-ballooning stability, it could be shown that initially the plasmas were PB unstable, but that with developing XPR height the growth rates of the most unstable toroidal modes severely decreased which lead to PB stability as well.

Chapter 7

Summary and Outlook

The X-point Radiator offers a regime that features a detached divertor, a high radiation fraction of up to almost 100% and an ELM-free operation at minimal plasma confinement degradation.[23] The scope of this thesis was to investigate the behaviour of the plasma in terms of its parameter evolution and MHD stability with respect to the XPR height.

In terms of the plasma parameter analysis, 95 time windows of 225 ms length were selected within seven discharges. The reason for the selection of discharges was that the highest number of plasma shots with an XPR exist for a plasma current of 800 kA and a B-field of -2.5 T. These time windows had similar values in heating, deuterium gas puff, q_{95}, plasma current and toroidal magnetic field. The analysed data consisted of the plasma parameter profiles, their respective gradient and gradient lengths. These profiles were provided through a standardised approach (IDA) that utilises several electron and ion property measurement diagnostics and their corresponding uncertainties based on Bayesian probability theory. The range of interest within this study reached from the outer-core to the separatrix ($\rho_{pol} \in [0.7; 1]$) and was split into 4 subregions which were chosen based on having a constant gradient within. The final step of the data preparation consisted of the temporal (each time window) and spatial (each subregion) averaging in order to derive a data point representing a specific time window and subregion within this study.

The investigation of the plasma stability was carried out on the basis of calculations with the codes HELENA and MISHKA for 10 time windows out of the discharges #36655, #38116 and #39004. HELENA provides local information on the ballooning stability and MISHKA the global peeling-ballooning stability. HELENA derives the critical normalised pedestal pressure gradient based on the experimental α as well as the magnetic shear for flux surfaces in the region $\rho_{pol} \in [0.9; 1]$. These values are used to determine, first, the marginal ballooning stability factor (F_{marg}, the ratio of experimental to critical α) and, second, in combination with magnetic shear, the operational point in the s-α-stability phase space. MISHKA utilises the equilibria generated by HELENA to produce the peeling-ballooning stability boundary within the j-α diagram and locate the operational point within the phase space.

In five of the analysed discharges the plasma went into an ELM-free regime when an XPR height of 7 cm was reached. This ELM-free access condition applies to discharges with a plasma current of 800 kA and a magnetic field of -2.5 T. The analysis concluded that the electron and ion temperature in the pedestal declined linearly for increasing XPR height showing no change in behaviour when the XPR reached a height of 7 cm. The density in the pedestal, on the other hand, stays fairly constant up to an XPR height of 5 cm and then decreases strongly also not showing significant affect of the plasma becoming ELM-free. The regions

inside the pedestal (region A-C) behave differently, both in density and temperature. It can be observed that the temperature initially decreases up to an XPR height of 5 cm after which it remains at the reduced levels. At the same time the temperature gradients in the inner regions increase. The density increases in this region and shows a maximum value at 4-5 cm which is followed by a descent to the reference values. In summary the pedestal is not affected by the entering of the ELM-free regime, whereas the temperatures in subregions A-C stabilize. A clear change in profile development occurs at an XPR height of 4-5 cm, which is correlated to low divertor temperature estimates from divertor shunt current measurements. This can be interpreted as a transition to detached target plates and subsequently a change in the recycling behaviour, serving as a plausible cause for the change in density.

The density gradient in the subregions situated between the pedestal and the outer core increase substantially, which could be the cause for a reduction in turbulence and therefore the reduced heat transport in this region. A detailed analysis of the dominant turbulent transport and how it is affected by the density gradient would be the topic of future work. The pressure values combine the findings in density and temperature. Plasma pressure inside the pedestal region stays unfazed despite a pedestal degradation due to a rapid recovery of the profile in between those regions. All subregions (except the pedestal) increase above the reference values (XPR height of 0 cm) following the course of the electron density and only as the XPR surpasses a height of 7 cm decrease marginally.

The MHD stability analysis concludes that the pedestal pressure gradient decreases sufficiently so that the plasma becomes ballooning and PB stable. This can be observed by the shift of the operational point away from the marginal ballooning stability limit in the s-α phase space and from the ballooning boundary in the j-α diagram.

The findings suggest that it is possible to operate the plasma in an ELM-free and divertor-detached regime with only slightly reduced core plasma conditions, therefore contributing towards the progress in engineering a future operational magnetic confinement fusion power plant.

Acknowledgement

Bibliography

[1] Friedlingstein P., et al. "Global Carbon Budget 2021". *Earth System Science Data*, 14(4):1917–2005, 2022.

[2] Masson-Delmotte V., et al. IPCC, 2021: Summary for Policymakers. In: "The Physical Science Basis. Contribution of Working Group I to the Sixth Assessment Report of the Intergovernmental Panel on Climate Change". resreport, IPCC, 2021.

[3] Mach K., et al. "Climate as a risk factor for armed conflict". *Nature*, 571(7764):193–197, 2019.

[4] United Nations Environment Programme. *Sudan Post-Conflict Environmental Assessment*. United Nations Environment Programme, United Nations Environment Programme, P.O. Box 30552, Nairobi, KENYA, June 2007. ISBN:978-92-807-2702-9.

[5] Fernando S.D. "Climate Change and Malaria - A Complex Relationship". *UN Chronicle*, 47(2):21–25, 2012.

[6] ITER Organization. "Advantages of fusion". `https://www.iter.org/sci/Fusion`, 2022. Accessed (01.07.2022).

[7] Khan M. A. *Nuclear astrophysics : a course of lectures*. CRC Press, Boca Raton, Fla, 2018.

[8] McCracken G. M & Stott P. E. *Fusion : the energy of the universe*. Complementary Science. Elsevier, Amsterdam, Netherlands, 2nd ed. edition, 2013.

[9] Ongena J. "Fusion: a true challenge for an enormous reward". *EPJ Web of Conferences*, 189:00015, 2018.

[10] Tokamak. `https://www.ipp.mpg.de/14869/tokamak`.

[11] Ham C., et al. "Filamentary plasma eruptions and their control on the route to fusion energy". *Nature Reviews Physics*, 2(3):159–167, 2020.

[12] Ikeda K. "Progress in the ITER Physics Basis". *Nuclear Fusion*, 47(6), 2007.

[13] Max Planck Institute for Plasma Physics. "ASDEX Upgrade". `https://www.ipp.mpg.de/1471827/asdex_upgrade`. Accessed (01.07.2022).

[14] Max Planck Institute for Plasma Physics. "ASDEX Upgrade". `https://www.ipp.mpg.de/16340/stand`. Accessed (01.07.2022).

[15] Max Planck Institute for Plasma Physics. "ASDEX Upgrade". `https://www.ipp.mpg.de/16208/einfuehrung`. Accessed (01.07.2022).

[16] Wagner F., et al. "Regime of Improved Confinement and High Beta in Neutral-Beam-Heated Divertor Discharges of the ASDEX Tokamak". *Phys. Rev. Lett.*, 49:1408–1412, 1982.

[17] Wagner F. "A quarter-century of H-mode studies". *Plasma Physics and Controlled Fusion*, 49(12B):B1–B33, 2007.

[18] Zohm H. "Edge localized modes (ELMs)". *Plasma Physics and Controlled Fusion*, 38(2):105–128, 1996.

[19] Loarte A., et al. "Chapter 4: Power and particle control". *Nuclear Fusion*, 47(6):S203, 2007.

[20] Wischmeier M. "High density operation for reactor-relevant power exhaust". *Journal of Nuclear Materials*, 463:22–29, 2015. PLASMA-SURFACE INTERACTIONS 21.

[21] Pacher G. W. "Modelling of DEMO core plasma consistent with SOL/divertor simulations for long-pulse scenarios with impurity seeding". *Nuclear Fusion*, 47(5):469–478, 2007.

[22] Tobita K. "Compact DEMO, SlimCS: design progress and issues". *Nuclear Fusion*, 49(7):075029, 2009.

[23] Bernert M., et al. "X-point radiation, its control and an ELM suppressed radiating regime at the ASDEX Upgrade tokamak". *Nuclear Fusion*, 61(2):024001, 2020.

[24] Senichenkov I. Y. et al. "Approaching the radiating X-point in SOLPS-ITER modeling of ASDEX Upgrade H-mode discharges". *Plasma Physics and Controlled Fusion*, 63(5):055011, 2021.

[25] Bernert M., et al. "Power exhaust by SOL and pedestal radiation at ASDEX Upgrade and JET". *Nuclear Materials and Energy*, 12:111–118, 2017. Proceedings of the 22nd International Conference on Plasma Surface Interactions 2016, 22nd PSI.

[26] Stacey W. M. *Fusion plasma physics*. Physics textbook. Wiley-VCH, Weinheim, 2nd ed.. edition, 2012.

[27] Okazaki T. *Fusion Reactor Design*. John Wiley & Sons Ltd., 2022.

[28] Mink A. F. *"Structure and Nonlinear Development of Edge Localized Magnetohydrodynamic Instabilities on the ASDEX Upgrade Tokamak"*. PhD thesis, Technical University of Munich, 2018.

[29] Zohm H. *Magnetohydrodynamic stability of tokamaks*. Wiley-VCH Verlag GmbH & Company KGaA, Weinheim, Germany, 2015.

[30] Connor J. W., Kirk A. & Wilson H. R. "Edge Localised Modes (ELMs): Experiments and Theory". *AIP Conference Proceedings*, 2008.

[31] Stroth U. *Plasmaphysik : Phänomene, Grundlagen und Anwendungen*. Springer Spektrum, Berlin, 2. auflage. edition, 2018.

[32] Connor J. W., et al. "Magnetohydrodynamic stability of tokamak edge plasmas". *Physics of Plasmas*, 5(7):2687–2700, 1998.

[33] Gohil P., et al. "Study of Giant Edge-Localized Modes in DIII-D and Comparison with Ballooning Theory". *Phys. Rev. Lett.*, 61:1603–1606, 1988.

[34] Peeters A. G. "The bootstrap current and its consequences". *Plasma Physics and Controlled Fusion*, 42(12B):B231, 2000.

[35] Connor J. W. "Edge-localized modes - physics and theory". *Plasma Physics and Controlled Fusion*, 40(5):531, 1998.

[36] Snyder P. B, et al. "Development and validation of a predictive model for the pedestal height". *Physics of Plasmas*, 16(5):056118, 2009.

[37] Snyder P.B., et al. "A first-principles predictive model of the pedestal height and width: development, testing and ITER optimization with the EPED model". *Nuclear Fusion*, 51(10):103016, 2011.

[38] Cathey A., et al. "Non-linear extended MHD simulations of type-I edge localised mode cycles in ASDEX Upgrade and their underlying triggering mechanism". *Nuclear Fusion*, 60(12):124007, 2020.

[39] Luda T., et al. "Integrated modeling of ASDEX Upgrade plasmas combining core, pedestal and scrape-off layer physics". *Nuclear Fusion*, 60(3):036023, 2020.

[40] Reimold F., et al. "Divertor studies in nitrogen induced completely detached H-modes in full tungsten ASDEX Upgrade". *Nuclear Fusion*, 55(3):033004, 2015.

[41] Hitzler F. *Radiative Cooling of the Divertor Plasma with Argon and Nitrogen Seeding in the ASDEX Upgrade Tokamak*. Dissertation, Technische Universität München, München, 2020.

[42] Pütterich T., et al. "Determination of the tolerable impurity concentrations in a fusion reactor using a consistent set of cooling factors". *Nuclear Fusion*, 59(5):056013, 2019.

[43] Kallenbach A. "Impurity seeding for tokamak power exhaust: from present devices via ITER to DEMO". *Plasma Physics and Controlled Fusion*, 55(12):124041, 2013.

[44] Casali L., et al. "Transport analysis of high radiation and high density plasmas in the ASDEX Upgrade tokamak". *EPJ Web of Conferences*, 79:01007, 2014.

[45] Carolan P. G. & Piotrowicz V. A. "The behaviour of impurities out of coronal equilibrium". *Plasma Physics*, 25(10):1065, 1983.

[46] Stangeby P. C. *The Plasma Boundary of Magnetic Fusion Devices*. Institute of Physics Publishing, 2000.

[47] Leonard A. W. "Plasma detachment in divertor tokamaks". *Plasma Physics and Controlled Fusion*, 60(4):044001, 2018.

[48] Kallenbach A., et al. "Partial detachment of high power discharges in ASDEX Upgrade". *Nuclear Fusion*, 55(5):053026, 2015.

[49] Kallenbach A., et al. "Electric currents in the scrape-off layer in ASDEX Upgrade". *Journal of Nuclear Materials*, 290-293:639–643, 2001. 14th Int. Conf. on Plasma-Surface Interactions in Controlled Fusion D evices.

[50] Chankin A.V., et al. "Parallel currents in the scrape-off layer of JET diverted discharges". *Journal of Nuclear Materials,* 196-198:739–744, 1992. Plasma-Surface Interactions in Controlled Fusion Devices.

[51] Bernert M. Power exhaust by SOL and pedestal radiation at ASDEX Upgrade and JET. In *22nd PSI, Rome,* 2016.

[52] Sommers H. P. *The ADAS user manual.,* 2004.

[53] Stroth U., et al. "Model for access and stability of the X-point radiator and the threshold for marfes in tokamak plasmas". *Nuclear Fusion,* 62(7):076008, 2022.

[54] Drake J. F. "Marfes: Radiative condensation in tokamak edge plasma". *The Physics of Fluids,* 30(8):2429–2433, 1987.

[55] Ryutov D. D., et al. "The 'churning mode' of plasma convection in the tokamak divertor region". *Physica Scripta,* 89(8):088002, 2014.

[56] Cavedon M., et al. "Experimental investigation of L- and H-mode detachment via the divertor Thomson scattering at ASDEX Upgrade". *Nuclear Fusion,* 62(6):066027, 2022.

[57] Pan O., et al. "SOLPS-ITER simulations of an X-point radiator in the ASDEX Upgrade tokamak". *Nuclear Fusion,* 63(1):016001, 2022.

[58] Viezzer E., et al. "High-accuracy characterization of the edge radial electric field at AS-DEX Upgrade". *Nuclear Fusion,* 53(5):053005, 2013.

[59] McDermott R. M., et al. "Extensions to the charge exchange recombination spectroscopy diagnostic suite at ASDEX Upgrade". *Review of Scientific Instruments,* 88(7):073508, 2017.

[60] Cruz-Zabala D.J., et al. "Upgrade of the edge Charge Exchange Recombination Spectroscopy system at the High Field Side of ASDEX Upgrade". *Journal of Instrumentation,* 14(11):C11006, 2019.

[61] Cavedon M., et al. "A fast edge charge exchange recombination spectroscopy system at the ASDEX Upgrade tokamak". *Review of Scientific Instruments,* 88(4):043103, 2017.

[62] Mlynek A., et al. "Design of a digital multiradian phase detector and its application in fusion plasma interferometry". *Review of Scientific Instruments,* 81(3), 2010. 033507.

[63] Suttrop W., Peeters A. G., ASDEX Upgrade team & NBI Group. "Practical Limitations to Plasma Edge ElectronTemperature Measurements by Radiometry ofElectron Cyclotron Emission". (IPP 1/306). Garching (DE): Max-Planck-Institut für Plasmaphysik., 1997.

[64] Rathgeber S. K., et al. "Estimation of edge electron temperature profiles via forward modelling of the electron cyclotron radiation transport at ASDEX Upgrade". *Plasma Physics and Controlled Fusion,* 55(2):025004, 2012.

[65] Willensdorfer M., et al. "Improved chopping of a lithium beam for plasma edge diagnostic at ASDEX Upgrade". *Review of Scientific Instruments,* 83(2), 2012. 023501.

[66] Willensdorfer M., et al. "Characterization of the Li-BES at ASDEX Upgrade". 56(2):025008, 2014.

[67] Brandenburg R., et al. "Modelling of fast neutral Li beams for fusion edge plasma diagnostics". *Plasma Physics and Controlled Fusion*, 41(4):471, 1999.

[68] Fischer R., et al. "Probabilistic lithium beam data analysis". *Plasma Physics and Controlled Fusion*, 50(8):085009, 2008.

[69] Schweinzer J., et al. "Reconstruction of plasma edge density profiles from Li I (2s-2p) emission profiles". *Plasma Physics and Controlled Fusion*, 34(7):1173, 1992.

[70] Schweinzer J., et al. "DATABASE FOR INELASTIC COLLISIONS OF LITHIUM ATOMS WITH ELECTRONS, PROTONS, AND MULTIPLY CHARGED IONS". *Atomic Data and Nuclear Data Tables*, 72(2):239–273, 1999.

[71] Kurzan B. & Murmann H. D. "Edge and core Thomson scattering systems and their calibration on the ASDEX Upgrade tokamak". *Review of Scientific Instruments*, 82(10), 2011. 103501.

[72] Kurzan B., et al. "Signal processing of Thomson scattering data in a noisy environment in ASDEX Upgrade". *Plasma Physics and Controlled Fusion*, 46(1):299, 2003.

[73] Fischer R., et al. "Integrated Data Analysis of Profile Diagnostics at ASDEX Upgrade". *Fusion Science and Technology*, 58(2):675–684, 2010.

[74] Mc Carthy PJ. "Analytical solutions to the Grad–Shafranov equation for tokamak equilibrium with dissimilar source functions". *Physics of Plasmas*, 6(9):3554–3560, 1999.

[75] Mc Carthy PJ and the ASDEX Upgrade Team. "Identification of edge-localized moments of the current density profile in a tokamak equilibrium from external magnetic measurements". *Plasma Physics and Controlled Fusion*, 54(1):015010, 2011.

[76] Fischer R., et al. "Magnetic equilibrium reconstruction using geometric informationfrom temperature measurements at ASDEX upgrade". In *40th EPS Conference on Plasma Physics*. European Physical Society, 2013.

[77] Radovanovic L. *Ballooning stability analysis of the ASDEX-Upgrade small-ELM regime*. PhD thesis, Wien, 2020.

[78] Huysmans G.T.A., Goedbloed J.P., Kerner W., et al. "Isoparametric bicubic Hermite elements for solution of the Grad-Shafranov equation". *Int. J. Mod. Phys. C*, 2(1):371–376, 1991.

[79] Konz C., and Zille R. HELENA-Fixed boundary equilibrium solver. *Max-Planck-Institut für Plasmaphysik, Garching*, 2007.

[80] Galvão R.M.O. & Rem, J. Application of the suydam method to the balloonings stability problem. *Computer Physics Communications*, 22(4):399–402, 1981.

[81] Laggner F. *Inter-ELM pedestal structure development in ASDEX Upgrade.* PhD thesis, 2017.

[82] Mikhailovskii A.B., et al. "Optimization of computational MHD normal-mode analysis for tokamaks". *Plasma Physics Reports*, 23, 1997.

[83] Huysmans G.T.A., et al. "Modeling of diamagnetic stabilization of ideal magnetohydrodynamic instabilities associated with the transport barrier". *Physics of Plasmas*, 8(10):4292–4305, 2001.

[84] Konz C., et al. "First physics applications of the Integrated Tokamak Modelling (ITM-TF) tools to the MHD stability analysis of experimental data and ITER scenarios". In *38th EPS Conference on Plasma Physics*. European Physical Society, 2011.

Appendices

The following graphic 1 illustrates the plasma parameter subregion behaviour in terms of the ρ_{pol} of the XPR. The course of the different profiles shows a non-linear behaviour to the XPR position in contrast to the when plotted against the XPR vertical position. This illustrates the non-linear effect of the XPR penetration with regard to its poloidal location. The observations throughout the plasma parameter subregion behaviour on XPR vertical height analysis do apply here as well although the magnitude of some findings might vary. The XPR height of 4 cm coincides with an XPR ρ_{pol} position of 0.998 and the 7 cm of XPR height to a ρ_{pol} position of 0.9975. This illustrates again the high flux expansion in the X-point vicinity.

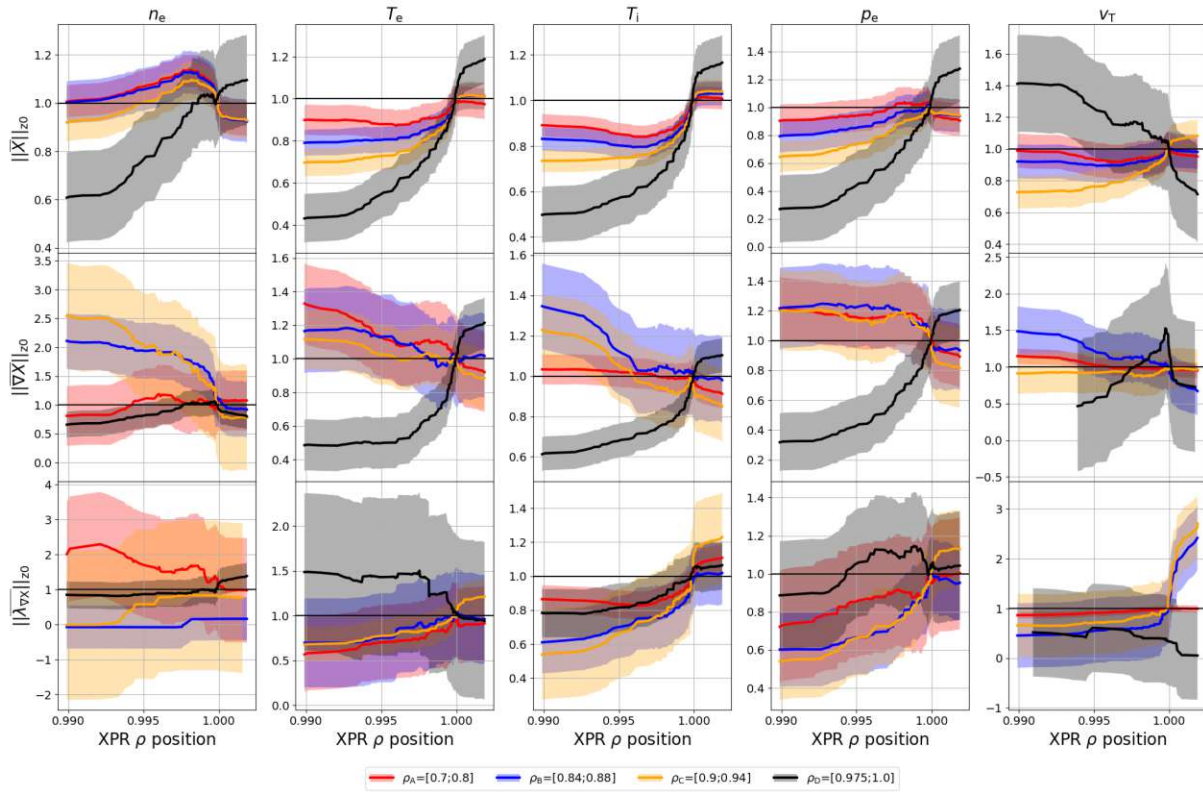Figure 1: The plasma parameter subregion analysis for an XPR penetration of 11 cm in terms of the ρ_{pol} location of the XPR.